

Investigating the potential of WO_3 and WS_2 as Cd-free buffer layers in Sb_2Se_3 -Based thin-film solar cells: A numerical study with SCAPS-1D software

Khulood Jamal Abbas*, Amir Bahrami*

Department of Physics, Ahvaz Branch, Islamic Azad University, Ahvaz, Iran



ARTICLE INFO

Keywords:

Thin-film solar cells
 Sb_2Se_3
 WO_3 and WS_2 buffer layers
SCAPS-1D simulation
Efficiency

ABSTRACT

In this numerical study, the performance of thin-film solar cells (TFSCs) based on Sb_2Se_3 with WO_3 and WS_2 materials as Cd-free buffer layers was investigated using SCAPS-1D software. WO_3 and WS_2 were chosen for their suitable band gaps, good electrical conductivity, and optical transparency. The proposed solar cell structures, Au/ Sb_2Se_3 / WO_3 /ITO and Au/ Sb_2Se_3 / WS_2 /ITO were theoretically examined, considering various factors such as conduction band offset, absorber and buffer layer thickness, doping concentrations, series and shunt resistances, temperature, activation energy, and C-V characteristic. The conduction band offset at the absorber/buffer interface showed spike-like configurations, with values of 0.38 eV and 0.23 eV for the WO_3 and WS_2 buffer layers, respectively. The optimized thickness for the absorber layer in both structures was 1 μm , while for WO_3 and WS_2 buffer layers, it was 0.1 μm and 0.05 μm , respectively. The optimized acceptor and donor doping concentrations were $1 \times 10^{16} \text{ cm}^{-3}$ and $1 \times 10^{18} \text{ cm}^{-3}$, respectively. The efficiency of the proposed photovoltaic devices was found to be 9.538 % (with $V_{oc} = 0.561 \text{ V}$, $J_{sc} = 30.856 \text{ mA/cm}^2$, $FF = 55.84 \%$) and 10.151 % (with $V_{oc} = 0.558 \text{ V}$, $J_{sc} = 29.189 \text{ mA/cm}^2$, $FF = 62.34 \%$) for structures with WO_3 and WS_2 buffer layers, respectively. These results suggest that using non-toxic materials like WO_3 and WS_2 as buffer layers can be an efficient and environmentally friendly alternative to toxic CdS for fabricating cost-effective and highly efficient Sb_2Se_3 -based TFSCs.

1. Introduction

Solar cells, due to advantages such as cost-effective performance, minimal pollution, long lifetime, ease of use, and low maintenance, attract global attention as a potential future energy source. Thin-film solar cells (TFSCs), owing to their excellent conversion efficiency, cost-effective materials, and simple production processes, stand out as potential competitors in the field of photovoltaic energy production [1]. Sb_2Se_3 , belonging to the V_2VI_3 family of non-organic binary compounds, is proposed as a *p*-type semiconductor with an appropriate energy band gap of 1 eV (indirect) and 1.5 eV (direct). The energy bandgap is the energy difference between solid materials' maximum valence band and the minimum conduction band. It possesses favorable attributes such as low toxicity, cost-effectiveness in manufacturing, abundance in the Earth's crust, high electrical conductivity, a high absorption coefficient ($>10^5 \text{ cm}^{-1}$), long carrier lifetime, suitable carrier mobility, and long-term stability. Due to these advantageous characteristics,

Sb_2Se_3 is acknowledged as a promising material for serving as a light-absorbing layer in TFSCs [2–4]. Numerous theoretical and experimental investigations have been conducted to assess the performance of Sb_2Se_3 solar cells, with extensive efforts directed toward enhancing their efficiency. While Sb_2Se_3 is commonly employed as an absorber material in TFSCs, ongoing research is focused on exploring new materials and optimizing buffer layers and structural aspects of solar cells. These endeavors aim to further improve the overall performance of Sb_2Se_3 -based solar cells.

Among TFSCs based on Sb_2Se_3 , various experimental devices have been fabricated to optimize power conversion efficiency (PCE). Notably, CdS has been employed as a buffer layer material in studies. Messina et al. [5], in 2009, achieved a PCEs of 0.66 % using CdS as a buffer layer. Subsequent advancements were reported by Zhou et al. [6] and Choi et al. [7], who achieved experimental PCEs of 2.26 % and 3.21 %, respectively, in 2014, using TiO_2 as a buffer layer. Wang et al. reported an experimental PCEs of 5.93 % in 2017, employing ZnO as buffer layers

* Corresponding author.

E-mail addresses: bahrami_amir@yahoo.com, bahrami.amir@iau.ac.ir (A. Bahrami).

[8], while Chen et al. achieved PCEs of 6.5 % with CdS as buffer layers [9]. Wen et al. demonstrated an efficiency of 7.6 % in 2018 using a vapor-deposited Sb_2Se_3 film and a CdS buffer layer [10]. In 2019, the highest reported experimental efficiency for Sb_2Se_3 TFSCs reached 9.2 %, with CdS as the buffer layer [11]. Despite these advancements, the achieved efficiencies in various configurations of experimentally fabricated thin-film Sb_2Se_3 solar cells remain below the Shockley–Queisser limit of 32 % [12].

Several theoretical studies have aimed to enhance the performance of Sb_2Se_3 -based solar cells, presenting diverse configurations. Theoretical results indicate an efficiency (η) of 16.5 % for the structure FTO/CdS/ Sb_2Se_3 /Au incorporating a CdS buffer layer [13]. Theoretical optimization with CdS as a buffer layer and carbon nanotubes (CNT) as the back electrode has yielded an optimal efficiency of 21.67 % [14]. Furthermore, a solar cell configuration (FTO/CdS/ Sb_2Se_3 /HTL/Au) utilizing CuO as the hole transport layer (HTL) has been theoretically estimated to achieve an efficiency of 23.18 % [15]. Another theoretical approach involving ZnSe as a buffer layer and AgInTe₂ as the HTL in the Sb_2Se_3 solar cell indicates an efficiency of 19.8 % [16]. In the work by Mamta et al., an Sb_2Se_3 /CdS/ZnO solar device incorporating a CdS buffer layer achieved an impressive efficiency of 27.84 % [17]. Another study by Mamta et al. reported an efficiency of 24 % for Sb_2Se_3 -based solar cells utilizing a ZnSe buffer layer [18]. Al Ahmad et al., investigated Sb_2Se_3 solar cells with CdS as the buffer layer and BaSi2 as the back surface layer (BSF), achieving the highest efficiency of 29.35 % [19]. In a study by Basak et al., Sb_2Se_3 solar cells with CdS as the buffer layer demonstrated an optimal device efficiency of 12.62 % [20]. Baig et al. found the highest efficiency of 13.20 % in Sb_2Se_3 solar cells by employing In_2S_3 , Cu_2O , and CNT as a buffer layer, HTL, and back electrode, respectively [21]. Recently, Kumari et al. reported an efficiency of 28.25 % in Sb_2Se_3 solar cells with a CdS buffer layer and SnTe as the HTL [22]. Additionally, an investigation by Sunny et al. shows an efficiency of 29.89 % in Sb_2Se_3 solar cells utilizing a CdS buffer layer and SnS as the HTL [23]. Wang X. et al. Reported the highest efficiency of 3.9 % for Sb_2Se_3 solar cells when incorporating CdS, TiO_2 , and double buffer layers (CdS/ TiO_2) [24]. Several studies have investigated the impact of different materials, including Si [25], CdSe [26], ZnS [27], ZnTe [28], CdS:O and WS₂ [29], Zn(O, S) [30], CdS/ZnS [31], $\text{TiO}_2/\text{Zn}_{0.93}\text{Mg}_{0.07}\text{O}$ and $\text{TiO}_2/\text{ZnO}_{0.4}\text{S}_{0.6}/\text{Zn}_{0.93}\text{Mg}_{0.07}\text{O}$ [32] cubic silicon carbide (3C-SiC) [33], Cd_{0.75}Zn_{0.25}S [34], CdZnS and SnO₂/CdZnS [35], Zn_{0.8}Sn_{0.2}O [36], and ZrS₂ [37]. However, despite these efforts, the reported theoretical efficiencies for various configurations of Sb_2Se_3 -based solar cells still fall below the Shockley–Queisser limit [12].

In general, the buffer layer is an essential component in the structures of TFSCs, playing a critical role in optimizing the device's performance. A buffer layer, using an *n*-type semiconductor material, is employed to create a p-n junction with a *p*-type semiconductor material. The buffer layer acts as a bridge for transporting charge carriers generated in the absorber layer to the electrode. The buffer layer needs to possess characteristics such as low electrical resistance, excellent optical transparency, and the ability to function as an accelerator for the generation of charge carriers in the absorber layer [38]. The buffer layer should possess a wide bandgap to facilitate the passage of photons through itself [39]. As photons pass from the buffer layer towards the absorber layer, various types of losses occur due to lattice mismatch and band alignment. Lattice mismatch and band alignment play a crucial role in determining the efficiency of a solar cell, influenced by interface defects, band alignment, and Fermi-level pinning [40,41]. CdS is a commonly employed buffer layer in TFSCs, particularly in Sb_2Se_3 -based solar cells [10,11,23,42]. However, this material contains a significant amount of Cd, which is a toxic element. Consequently, researchers have shifted their focus to investigating alternative materials suitable to CdS for incorporation in buffer layers. Recently, tungsten trioxide (WO₃) and tungsten disulfide (WS₂) have emerged as excellent buffer layer candidates and potential substitutes for toxic CdS material in TECs [39, 43–45]. WO₃ is an *n*-type semiconductor with chemical stability and an

adjustable bandgap within the wide range of approximately 2.6–3.5 eV. It is a non-toxic, easily producible, and cost-effective material, exhibiting 80 % transmission in the visible region. Moreover, WO₃ exhibits good electron mobility, and its state density and Fermi level can be controlled by adjusting the oxygen content during production and processing. Furthermore, WO₃ demonstrates a commendable conductivity at approximately $\sim 10^{-3} \Omega^{-1}\text{cm}^{-1}$, along with possessing *n*-type semiconductor properties. Generally, WO₃ is employed as an electron transport layer (ETL) in the design of solar cells [38,46–48]. Furthermore, transition metal dichalcogenides (TMDCs), such as tungsten disulfide (WS₂), have attracted significant attention for photovoltaic applications due to their distinctive electrical, optical, and electrochemical properties. WS₂, as an earth-abundant element, is a direct band gap semiconducting material that is non-toxic. Moreover, WS₂ displays high carrier mobility and good conductivity ($\sim 10^{-3} \Omega^{-1}\text{cm}^{-1}$) and attends as an *n*-type semiconductor [49–51]. Both WO₃ and WS₂ thin films can be fabricated through various techniques such as chemical vapor deposition (CVD), chemical vapor transport (CVT), physical vapor deposition (PVD), atomic layer deposition (ALD), and spray coating [52–56].

In this present work, thin-film photovoltaic devices with structures Au/ Sb_2Se_3 /WO₃/ITO and Au/ Sb_2Se_3 /WS₂/ITO based on Sb_2Se_3 have been proposed, modeled, and numerically simulated. WO₃ and WS₂ materials have been used instead of CdS as the electron transport layer (buffer layer). The simulation software SCAPS-1D has been employed to investigate the performance of the proposed devices. Initially, the model's validity was carried out through a comparative study of the reproduction of the parameters of an experimental Sb_2Se_3 -based solar cell with utilities CdS as a traditional buffer layer within the simulation environment. Then, the impact of replacing CdS with WO₃ and WS₂ on the CBO and VBO relationships in the ETL/absorber interface was studied. In the next stage, a systematic analysis of the physical input parameters for both proposed structures, such as thicknesses and carrier concentration in the absorber and buffer layers, was analyzed. The optimization of WO₃ and WS₂ buffer layer parameters was explored to maximize device performance. Also, the study assessed the influence of series and shunt resistances, operating temperature, activation energy, back metal work function, and the Mott–Schottky diagram on the performance of both proposed solar cell structures. Therefore, through the optimization of physical parameters in TFSCs and employing appropriate simulations, experimental research can be guided toward the development of cost-effective and more efficient solar cells.

2. The structure of the device and methodology for simulation

2.1. The structure of the device of the Sb_2Se_3 -based solar cell

The main configuration of the Sb_2Se_3 -based solar cell consists of a sequence of thin layers, including a front contact, buffer layer, absorber layer, and back contact. Fig. 1 presents a schematic diagram of the Sb_2Se_3 heterojunction solar cells simulated in our study. Fig. 1 (a) shows the schematic structure of conventional TFSCs based on Sb_2Se_3 (Au/ Sb_2Se_3 /CdS/ITO). In this heterojunction structure, Sb_2Se_3 are *p*-type semiconductors as the absorbent layer, and CdS acts as an *n*-type semiconductor in the buffer layer (electron transporter), forming the p-n junction to collect photogenerated carriers (electron-hole pair). ITO (SnO₂:In) is utilized as a front contact (or window layer) due to its high conductivity, transparency, and low cost for collecting electron carriers, while Au is a back contact for collecting hole carriers. Fig. 1 (b) illustrate the proposed heterojunction structure of TFSCs based on Sb_2Se_3 with the configuration Au/ Sb_2Se_3 /(WO₃ or WS₂)/ITO. In this configuration, WO₃ and WS₂ as *n*-type semiconductor buffer layers, replacing the conventional CdS layer.

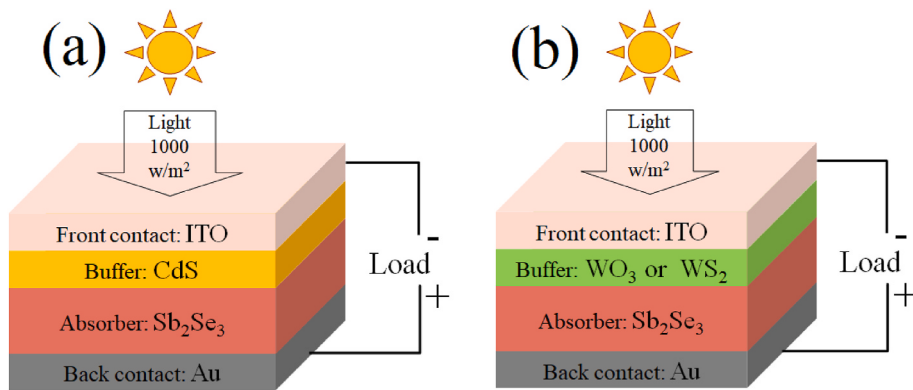


Fig. 1. Schematic structure of the studied Sb_2Se_3 solar cells: (a) conventional cell $\text{Au}/\text{Sb}_2\text{Se}_3/\text{CdS}/\text{ITO}$ and (b) proposed cells $\text{Au}/\text{Sb}_2\text{Se}_3/\text{WO}_3$ or WS_2/ITO .

2.2. Numerical modeling and methodology for simulation

We employed the Solar Cell Capacitance Simulator (SCAPS) version 3.3.10 for our simulations. SCAPS is an open-source software developed by Marc Burgelman and his team at the University of Gent, Belgium [57]. The SCAPS-1D simulation software is capable of solving a set of three ordinary differential equations, which include the Poisson equation, the carrier transport equation (drift-diffusion equation), and the continuity equations for electrons and free holes. This software numerically solves these equations under one-dimensional conditions and stable states with appropriate boundary conditions. Through this numerical approach, SCAPS-1D calculates the electrical characteristics of solar devices. These data are instrumental in analyzing and optimizing the performance of solar devices and facilitating significant improvements in their design [58]. To simulate and analyze the performance of the proposed TFSc using the SCAPS-1D software, it is essential to consider various physical parameters of different layers. These parameters have been collected from previously experimental and

computational reports and are listed in Table 1 [14,16,42,50,59,60]. Moreover, input parameters for the front and back contacts are presented in Table 2. In contrast, the defect density parameters in the absorber and buffer layers and the interfaces are shown in Table 3. To simplify numerical calculations in the SCAPS-1D software, it is assumed that the thermal velocities of electrons and holes in semiconductors remain constant at 10^7 cm/s at room temperature. Additionally, a surface recombination velocity of 10^7 cm/s has been chosen for both electron and hole carriers in the front and back contact layers. The simulations were conducted under standard test conditions for the sunlight spectrum, A.M 1.5 G (1000 W/m^2), and a temperature of 300 K. Nevertheless, our work also explored the influence of temperature on the efficiency of the proposed solar cell. Moreover, for the initial assumptions in the simulations, the series resistance and shunt resistance of the solar cells were considered zero and infinitely large, respectively [19].

3. Results and discussion

3.1. Validation of Sb_2Se_3 -based solar cell simulated with experimental work

Before beginning the modeling and optimization of the suggested solar cells, for validation and comparison of our work, we first reproduce and compare the experimental results of a Sb_2Se_3 -based solar cell with a CdS buffer layer, as reported by Wen et al. [10]. As observed in Fig. 2, the J-V characteristic curves for both the experimental and simulated results exhibit good agreement (experimental data extracted from the reported figure by Wen et al. [10], using the Digitizer tool in Origin Pro software).

Table 4 presents the output parameters obtained from reproducing the experimental and simulated results. We obtained a $V_{oc} = 0.425 \text{ V}$, $J_{sc} = 30.623 \text{ mA/cm}^2$, $FF = 58.245 \%$, and a $\eta = 7.580 \%$ for the simulated solar cell. These values closely match the experimental values reported by Wen et al. [10], demonstrating good agreement between the simulation and experimental results. Based on Eq. (1), the observed deviations (Δ) for V_{oc} , J_{sc} , FF , and η are only 1.19 %, 2.41 %, 3.56 %, and 1.06 %, respectively (refer to Table 4). These results indicate that the photovoltaic parameters used for simulation in the SCAPS software are

Table 1
The material parameters of the proposed model are used in SCAPS simulations.

Parameters (unit)	ITO	Absorb $p\text{-}\text{Sb}_2\text{Se}_3$	Buffer		
			$n\text{-CdS}$	$n\text{-}\text{WO}_3$	$n\text{-}\text{WS}_2$
Thickness (μm)	0.1	0.5–3.0	0.070	0.05–0.3	0.05–0.3
Bandgap (eV)	3.6	1.19	2.42	3.2	2.1
Electron affinity (eV)	4.5	4.18	4.4	3.8	3.95
Relative dielectric permittivity	8.9	14.5	10	12	13.6
CB effective density of states (cm^{-3})	2.2×10^{18}	2.0×10^{18}	1.2×10^{18}	1.8×10^{19}	2.0×10^{18}
VB effective density of states (cm^{-3})	1.8×10^{19}	1.0×10^{19}	1.8×10^{19}	7.1×10^{19}	2.0×10^{19}
Electron thermal velocity (cm/s)	1×10^7	1×10^7	1×10^7	1×10^7	1×10^7
Hole thermal velocity (cm/s)	1×10^7	1×10^7	1×10^7	1×10^7	1×10^7
Electron mobility ($\text{cm}^2 \text{ V}^{-1} \text{ s}^{-1}$)	10	16.70	100	40	100
Hole mobility ($\text{cm}^2 \text{ V}^{-1} \text{ s}^{-1}$)	10	16.70	50	40	25
Donor doping N_D (cm^{-3})	1×10^{21}	0	$10^{16}\text{--}10^{20}$	$10^{16}\text{--}10^{20}$	$10^{16}\text{--}10^{20}$
Acceptor doping N_A (cm^{-3})	0	$10^{16}\text{--}10^{20}$	0	0	0
Radiative recombination coefficient (cm^3/s)	–	2.3×10^{-9}	–	–	–
Reference	[16, 42]	[42, 59]	[42]	[60]	[50]

Table 2
Parameters contact electrical properties utilized in this work.

Parameters (unit)	Front Contact	Back Contact
Metal of work function (eV)	Flat	4.5–5.6
Surface recombination velocity of electron (cm^{-2})	1.0×10^7	1.0×10^7
σ_e		
Surface recombination velocity of hole (cm^{-2})	1.0×10^7	1.0×10^7
σ_h		

Table 3

Defect density parameters in the absorber and buffer layers and the interfaces used in this work.

Parameters (unit)	Sb ₂ Se ₃	WO ₃	WS ₂	Sb ₂ Se ₃ /WO ₃	Sb ₂ Se ₃ /WS ₂
Defect type	Single Donor	Single Acceptor	Single Acceptor	Neutral	Neutral
Capture cross-section of electrons (cm ²)	4.7 × 10 ⁻¹²	1.0 × 10 ⁻¹⁵	1.0 × 10 ⁻¹⁵	1.0 × 10 ⁻¹⁶	1.0 × 10 ⁻¹⁶
Capture cross-section of holes (cm ²)	4.7 × 10 ⁻¹²	1.0 × 10 ⁻¹⁵	1.0 × 10 ⁻¹⁵	1.0 × 10 ⁻¹⁶	1.0 × 10 ⁻¹⁶
Reference for defect energy level E _t	above the highest E _v	above the highest E _v			
Energy with respect to reference (eV)	0.6	0.6	0.6	0.6	0.6
Total density (cm ⁻³)	1.0 × 10 ¹⁴	1.0 × 10 ¹⁵	1.0 × 10 ¹⁵	–	–
Total density interface (cm ⁻²)	–	–	–	3.5 × 10 ¹⁶	3.5 × 10 ¹⁶

consistent with the parameters of an actual device. Therefore, this provides a logical foundation for our research and analysis, confirming the validity of our model.

$$\Delta = \frac{|X_{\text{sim}} - X_{\text{exp}}|}{X_{\text{exp}}} \quad (1)$$

3.2. The impact of CBO and VBO at the absorber/buffer interface

According to Anderson's law, the vacuum levels corresponding to two different semiconductors on both sides of heterogeneous binding compounds must align in energy band diagrams. This alignment leads to a discontinuity between the two energy bands in the intermediate region [61]. In a heterojunction structure, the discontinuity between the energy bands of a semiconductor compound is called a band offset. These discontinuities arise from the difference in the energy band gaps between semiconductors and are categorized into two types: conduction band offset (CBO = ΔE_c) and valence band offset (VBO = ΔE_v). The difference in CBO between the absorber and the buffer layer in the type of junction created at the heterojunction semiconductor interface is crucial. As Fig. 3 shows, two types of positive and negative CBO are formed at the interface based on the sign, as indicated in Eq. (2) and Eq. (3) [61]:

$$CBO = \Delta E_C = \chi_{\text{Absorber}} - \chi_{\text{Buffer}} \quad (2)$$

$$VBO = \Delta E_V = (\chi + E_g)_{\text{Absorber}} - (\chi + E_g)_{\text{Buffer}} \quad (3)$$

A positive CBO sign indicates that the buffer layer's CB is higher than that of Sb₂Se₃, while a negative sign signifies that the buffer layer's CB is lower than that of Sb₂Se₃. In the solar cell structure with CdS as the conventional buffer layer (Fig. 3(b)), a negative CBO is observed (CBO = -0.22 eV). When CBO is negative, the energy band exhibits a "cliff-like" profile, leading to an accumulation of electrons near the Sb₂Se₃/CdS interface. This accumulation can accelerate carrier recombination, thereby impacting the performance of the device. In the proposed solar cell structures with WO₃ and WS₂ as the buffer layer (Fig. 3 c and d), a positive CBO of 0.38 eV is observed for the Sb₂Se₃/WO₃ interface and 0.23 eV for the Sb₂Se₃/WS₂ interface, respectively. When CBO is positive, a "spike-like" profile can form at the absorber/buffer layer's interface, preventing the recombination of light-generated carriers. Carriers with energy exceeding the offset value can overcome obstacles and detach, while carriers with insufficient energy are unable to traverse obstacles and recombination without separation. The VBO difference in the Sb₂Se₃/CdS interface of a conventional solar cell is -1.45 eV, while in the Sb₂Se₃/WO₃ and Sb₂Se₃/WS₂ interfaces of the proposed solar cells, it is determined to be -1.63 eV and -0.68 eV, respectively. The negative values for both proposed structures indicate that no hole carrier transfer occurs from the absorber layer to the buffer layer. This ensures an effective blocking of hole carriers at the interface [50].

3.3. Optimization of PV performance by varying layer parameters

To investigate the PCE of the proposed heterojunction solar cells Au/Sb₂Se₃/WO₃/ITO and Au/Sb₂Se₃/WS₂/ITO, we have optimized the relevant physical parameters of their various layers. These parameters include the thickness of both the absorber and buffer layers, as well as the doping concentration of both layers. Additionally, we have investigated the effects of series and shunt resistances, temperature, activation energy, back contact work function, and the C-V characterization. To simplify numerical computations in the SCAPS-1D program, we assumed that the defect density in the layers and the interface between the layers remain constant at room temperature, as specified in Table 1.

3.3.1. Effect of absorber and buffer layers thickness

The thickness of both the absorber and buffer layers in solar cells are two critical factors that significantly impact their performance. To

Table 4

Comparison of main photovoltaic parameters between experimental results and simulations, as well as the absolute error between them.

Research type	V _{oc} (V)	J _{sc} (mA/cm ²)	FF (%)	η (%)
Experimental	0.42	29.9	60.4	7.5
Simulation	0.245	30.623	58.245	7.580
Δ	1.19 %	2.41 %	3.56 %	1.06 %

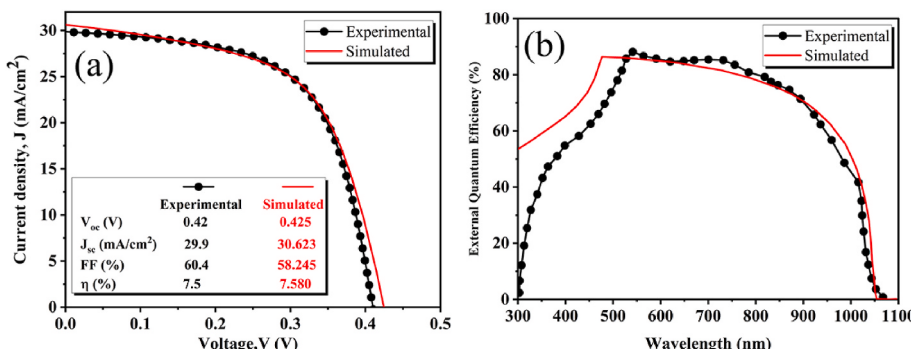


Fig. 2. The benchmarking of experimental and simulated Au/Sb₂Se₃/CdS/ITO solar cell device. (a) J-V curve and (b) EQE curve.

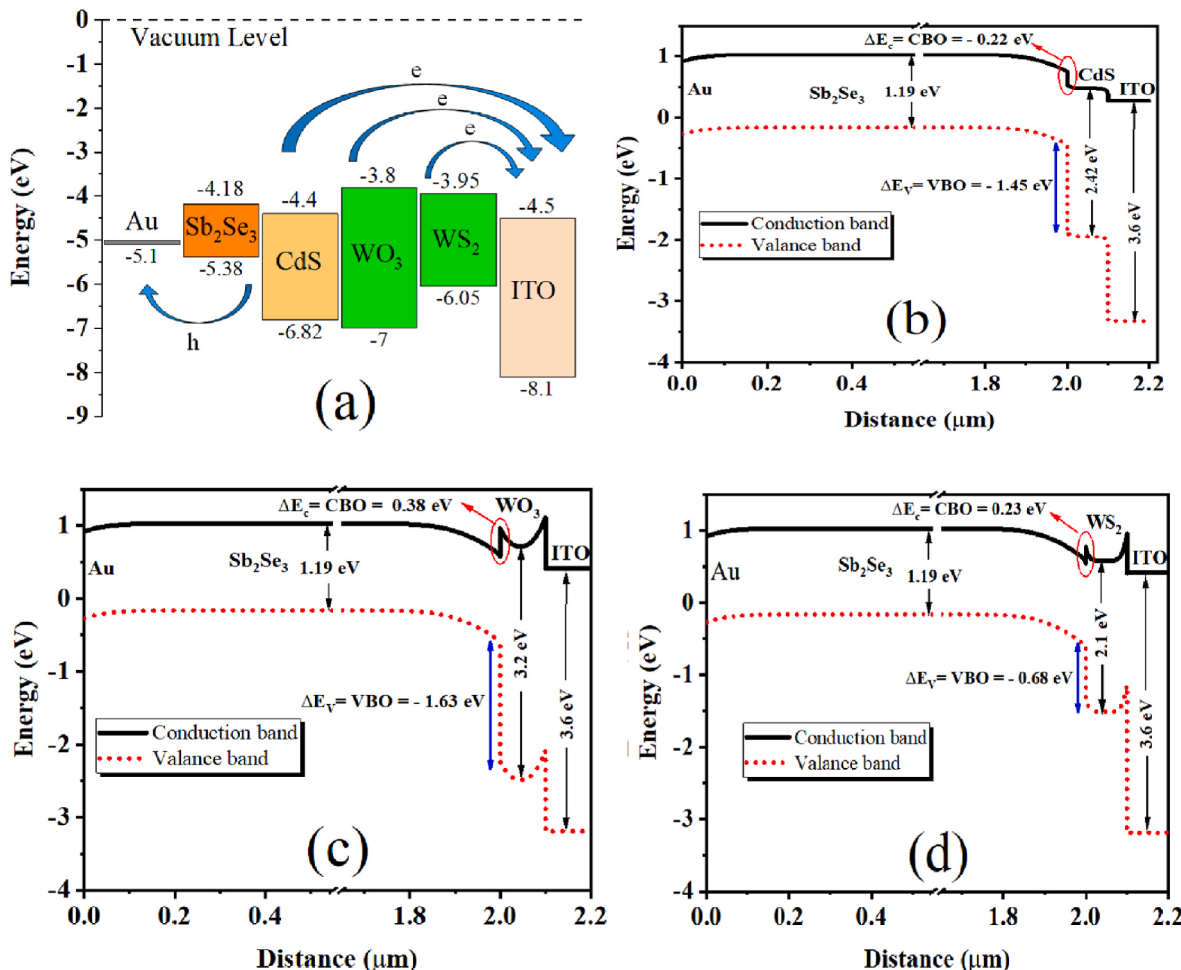


Fig. 3. (a) Schematic Energy band diagram of the studied Sb₂Se₃ solar cells and Simulated band diagram of (b) conventional cell Au/Sb₂Se₃/CdS/ITO, (c,d) proposed cells Au/Sb₂Se₃/(WO₃) or (WS₂)/ITO.

ensure optimal cell functionality, the thickness of these layers must be appropriately chosen. If the absorber layer is too thin, it may fail to sufficiently absorb light, resulting in insufficient energy production by the cell. Conversely, if the thickness of this layer is too high, it can lead to the generation of additional electrical current, causing the cell to lose efficiency. To optimize the proposed solar cells, in the first step, we

assessed the influence of both absorber and buffer layer thickness on the photovoltaic parameters. The Sb₂Se₃ absorber layer thickness was varied from 0.5 μm to 3 μm in 6 steps, and the WO₃ and WS₂ buffer layers' thickness ranged from 0.05 μm to 0.3 μm in 6 steps, while maintaining all other parameters constant according to Table 1. In Fig. 4, contour plots depicting the efficiency of the Au/Sb₂Se₃/WO₃/ITO and Au/

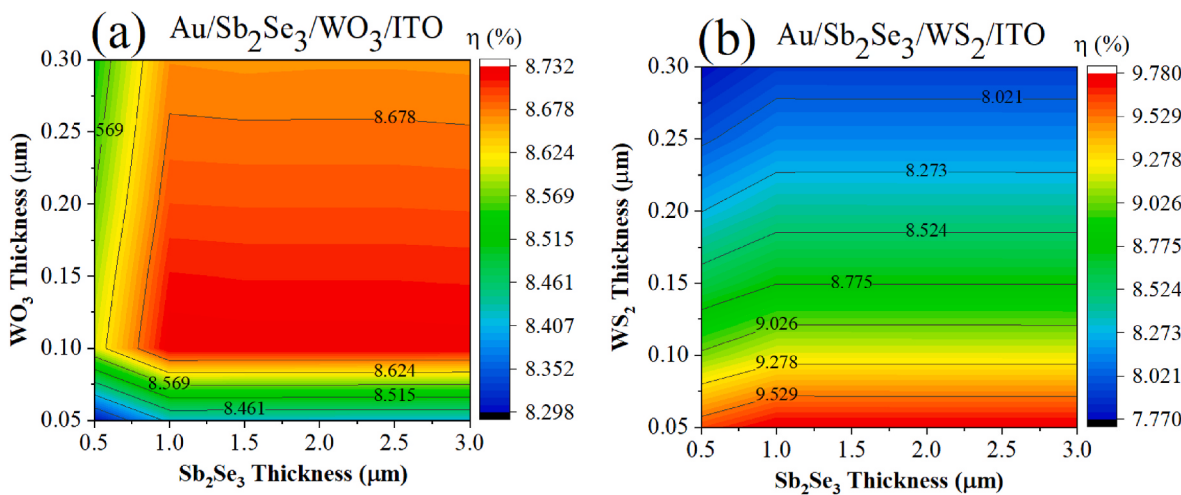


Fig. 4. Contour plots of variation of efficiency with thickness of the Sb₂Se₃ and the thickness of the WO₃ and WS₂ proposed solar cells (a) Au/Sb₂Se₃/WO₃/ITO (b) Au/Sb₂Se₃/WS₂/ITO.

$\text{Sb}_2\text{Se}_3/\text{WS}_2/\text{ITO}$ devices as functions of variations in the absorber and buffer layer thicknesses. Fig. 4 (a) and (b) show that variations in the thickness of both the absorber and buffer layers significantly impact the solar cell's efficiency. Maximum efficiency can be achieved by selecting a thickness of 1 μm for the absorber layer, 0.1 μm , and 0.05 μm for the WO_3 and WS_2 buffer layer, respectively.

To determine the optimal thickness of the absorber layer for both proposed solar cells, we plotted the impact of the absorber layer thickness on the photovoltaic parameters of the suggested solar cells, while maintaining the buffer layer thickness at 0.1 μm and 0.05 μm for the WO_3 and WS_2 buffer layer, respectively, and keeping all other physical parameters constant according to Table 1.

From Fig. 5 (a), it can be observed that with an increase in the absorber layer thickness, V_{oc} , J_{sc} , and η of the heterojunction $\text{Sb}_2\text{Se}_3/\text{WO}_3$ solar cell gradually increase. V_{oc} reaches its optimal value of 0.543 V at a thickness of 1 μm and then exhibits an almost constant trend. J_{sc} also shows a similar trend, with the optimum and maximum J_{sc} reaching 31.11 mA/cm^2 at a thickness of 1 μm . The PCE gradually increases, reaching a maximum of 8.73 % at a thickness of 1 μm , and then shows a relatively constant trend with an increase in the absorber layer thickness. The fill factor (FF) increases gradually from 50.54 % to 51.28 % as the absorber layer thickness changes from 0.5 μm to 1 μm and then shows an almost constant trend. As the absorber layer thickness increases, the internal resistance of the heterogeneous $\text{Sb}_2\text{Se}_3/\text{WO}_3$ solar cell also increases, making the charge-discharge process more challenging, resulting in a decrease in the fill factor. Analysis of Fig. 5 (a) suggests that the optimal thickness of the absorption layer for the heterojunction $\text{Sb}_2\text{Se}_3/\text{WO}_3$ solar cell is 1 μm .

As evident from Fig. 5 (b), in the $\text{Sb}_2\text{Se}_3/\text{WS}_2$ solar cell, with an increase in the absorber layer thickness from 0.5 to 3 μm , V_{oc} remains nearly constant, showing a value of 0.541 V. J_{sc} increases from thickness of 0.5–1 μm , reaching its maximum value ($29.885 \text{ mA}/\text{cm}^2$) at this thickness and then remains almost constant after 1 μm thickness. η also gradually increases within the thickness range of 0.5–1 μm , reaching its highest calculated value of 9.773 %, and then remains almost constant up to a thickness of 3 μm . However, FF exhibits a decreasing trend within the thickness range of 0.5–1 μm , reducing from 60.786 % to 60.503 %. As shown in Fig. 5 (b), the I-V output parameters remain almost constant beyond a thickness of 0.1 μm . Therefore, according to the simulated

results, for cost-effective production and achieving the highest efficiency for both proposed devices, the optimum thickness for the Sb_2Se_3 absorber layer is one 1 μm .

The optimal thickness of the buffer layers for both proposed devices is determined through simulation results of solar cell output parameters, plotted in Fig. 6. The thickness variation ranges from 0.05 μm to 0.3 μm . As observed in Fig. 6 (a), for the $\text{Au}/\text{Sb}_2\text{Se}_3/\text{WO}_3/\text{ITO}$ solar cell, an increase in the WO_3 buffer layer thickness leads to enhancements in V_{oc} , J_{sc} , FF, and η from 0.05 to 0.1 μm , reaching optimal values of 0.543 V, 31.109 mA/cm^2 , 51.70 %, and 8.73 %, respectively. Following this, V_{oc} , J_{sc} , and η exhibit a very slight decreasing trend, while FF remains relatively stable with no significant change. Thus, according to the simulation results, the maximum PCE is identified at a thickness of 1 μm . Hence, the optimal thickness for the WO_3 buffer layer in the proposed $\text{Au}/\text{Sb}_2\text{Se}_3/\text{WO}_3/\text{ITO}$ solar cell is chosen to be 1 μm . Fig. 6 (b) shows an increase in the WS_2 buffer layer thickness from 0.05 to 0.3 μm , resulting in a decrease in V_{oc} from 0.541 to 0.531 V and J_{sc} from 29.885 to 24.599 mA/cm^2 . Despite the decline in both V_{oc} and J_{sc} , with increasing thickness, FF shows an improvement from 60.503 % to 60.677 %. However, efficiency decreases from 9.773 % at a thickness of 0.05 μm –7.925 % at a thickness of 0.3 μm . Therefore, based on the simulation results, the maximum PCE is observed at a thickness of 0.05 μm . Hence, the optimal thickness for the WS_2 buffer layer in the proposed $\text{Au}/\text{Sb}_2\text{Se}_3/\text{WS}_2/\text{ITO}$ solar cell is determined to be 0.05 μm . The optimal values are associated with considering that a thicker buffer layer could cause the loss of more photons. As the thickness of the buffer layer increases, the number of photons that carry energy increases. With an increase in the buffer layer thickness, more photons carrying energy are absorbed, leading to fewer photons reaching the absorber layer and consequently generating fewer electron-hole pairs [62].

3.3.2. Impact on external quantum efficiency (EQE)

Fig. 7 presents the variations in external quantum efficiency (EQE) as a function of photon wavelength, considering changes in absorber and buffer layer thicknesses for both proposed solar cells. While visible light constitutes only a portion of solar radiation, energy from infrared (IR) and ultraviolet (UV) light exists across different spectrum regions. Developing solar cells capable of absorbing these wavelengths can significantly enhance electricity generation. Utilizing non-visible

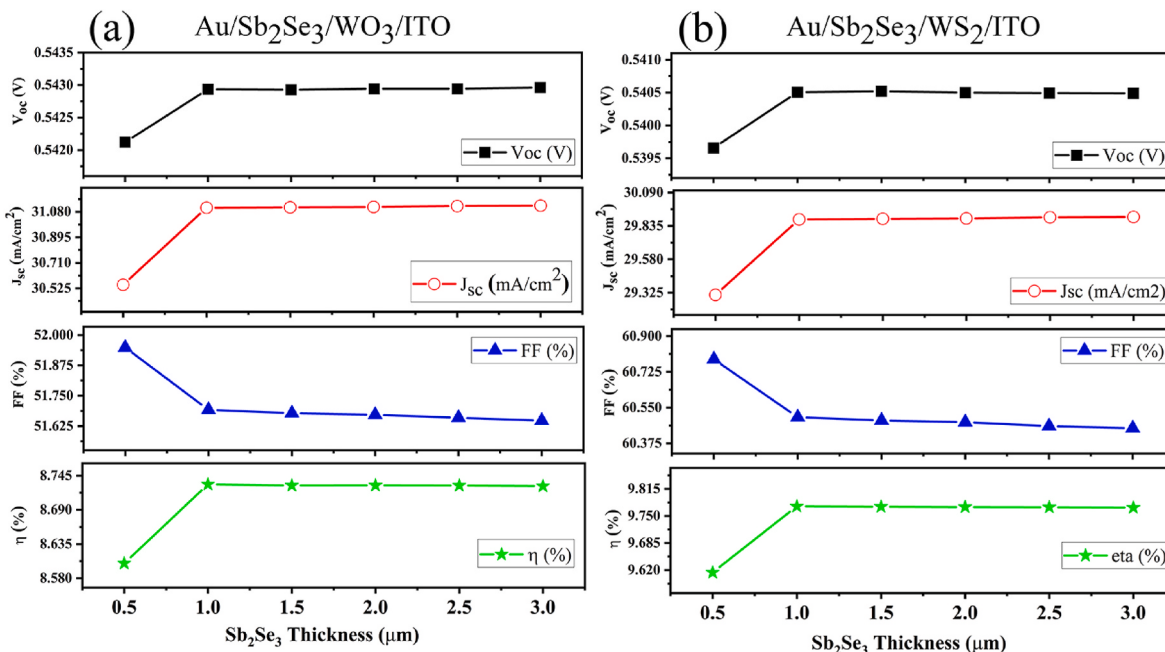


Fig. 5. Output of IV parameters with Sb_2Se_3 thickness for (a) $\text{Au}/\text{Sb}_2\text{Se}_3/\text{WO}_3/\text{ITO}$ and (b) $\text{Au}/\text{Sb}_2\text{Se}_3/\text{WS}_2/\text{ITO}$ devices.

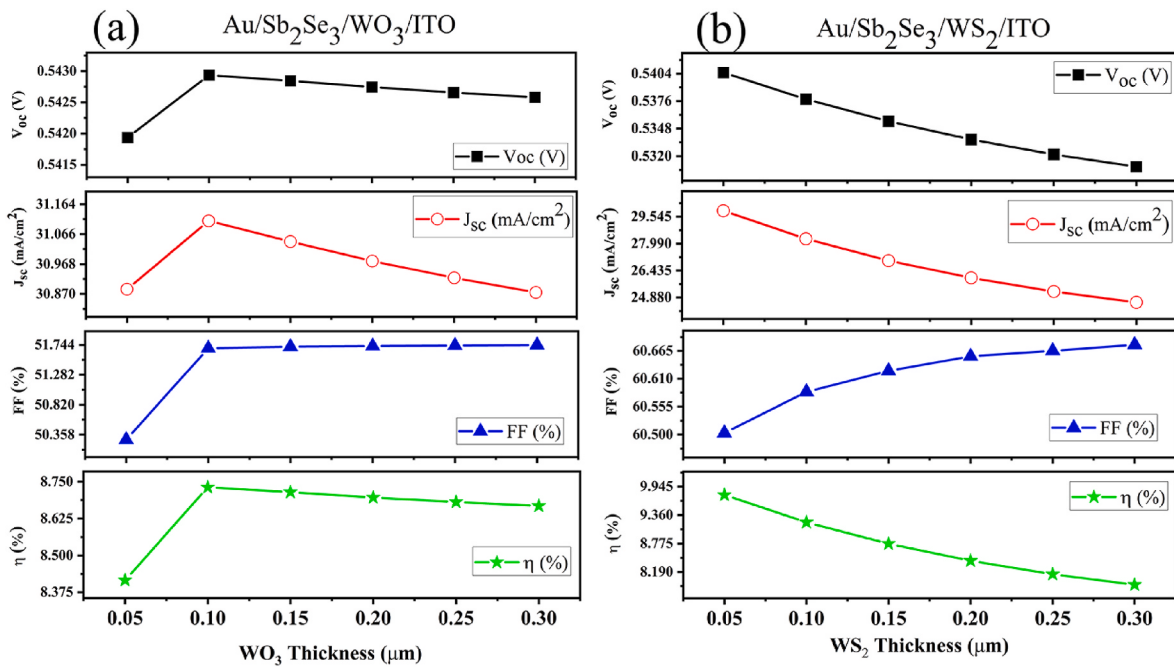


Fig. 6. Output of IV parameters with Buffer layer thickness for (a) $\text{Au}/\text{Sb}_2\text{Se}_3/\text{WO}_3/\text{ITO}$ and (b) $\text{Au}/\text{Sb}_2\text{Se}_3/\text{WS}_2/\text{ITO}$ devices.

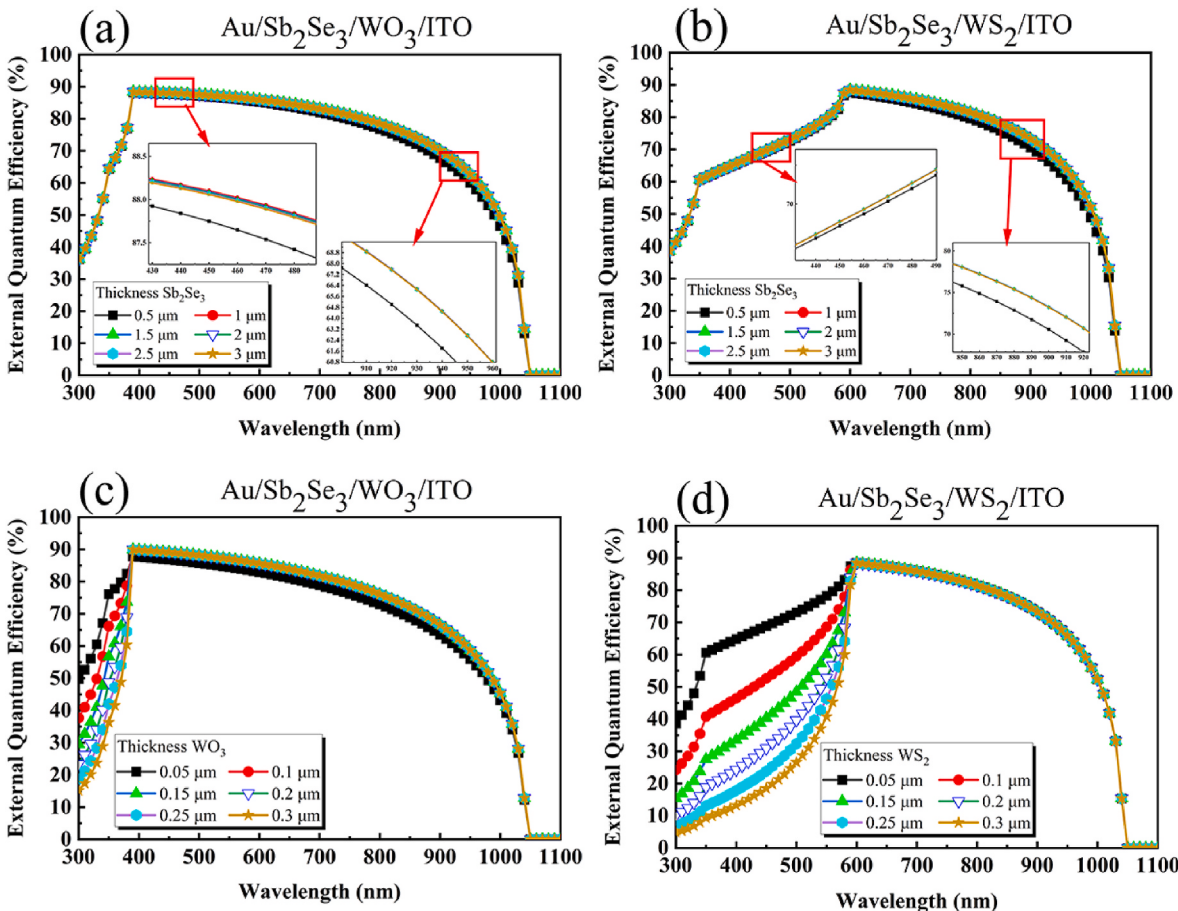


Fig. 7. (a and b) EQE behavior as a function of Sb_2Se_3 thickness, (c and d) EQE behavior as a function of WO_3 and WS_2 thickness for both proposed solar cell devices.

wavelengths offers a solution to surpassing the maximum theoretical efficiency limit (Shockley-Queisser limit), potentially leading to a revolutionary advancement in solar energy utilization. It could improve

overall solar cell efficiency, especially in regions with varying solar spectra due to weather conditions and time of day. Since infrared light emanates from heat sources within buildings, solar cells capable of

absorbing these wavelengths are of considerable interest to researchers. Furthermore, expanding studies beyond the visible spectrum enables the investigation of specific materials and emerging technologies. For instance, infrared-sensitive photovoltaic materials such as quantum dots, organic molecules, perovskites, multi-junction solar cells, and tandem solar cells have demonstrated the ability to convert IR light into electricity [63,64].

Fig. 7 (a) and (b) describe the effect of varying the absorber layer thickness on EQE for both proposed solar cells. As an increase in absorber layer thickness in the longer wavelengths (650–1000 nm), EQE experiences slight increases due to the enhanced photon absorption by the absorber layer. Notably, the solar cell with the WS_2 buffer layer exhibits a broader EQE spectrum compared to the solar cell with the WO_3 buffer layer. However, for thicker absorber layers exceeding 1 μm , EQE remains unchanged (refer to the inset **Fig. 7(a)** and (b)). In the shorter wavelength range (blue region), EQE is independent of the absorber layer thickness for both proposed solar cells. Nevertheless, at longer wavelengths, EQE diminishes toward zero percent. This phenomenon arises due to the photon energy being lower than the bandgap energy ($h\nu < E_g$), impeding the excitation of electrons from the valence band to the conduction band [65]. Additionally, **Fig. 7** (c) and (d) illustrate the influence of changing the thickness of the WO_3 and WS_2 buffer layers on EQE, respectively. In the short wavelength range (blue region), the effect of buffer layer thickness on the EQE curve is noticeable, showing a substantial decrease with increasing thickness for both WO_3 and WS_2 buffer layers. However, at longer wavelengths, there is no significant difference in external quantum efficiency for both proposed solar cells. Since photons with shorter wavelengths are more absorbed near the surface, thinner WO_3 and WS_2 buffer layers will absorb more photons effectively, allowing for better photon collection compared to thicker layers. This behavior is similar to that of the Sb_2Se_3 -based solar cells with CdS and ZnS [31] and ZnSe [66] buffer layers.

3.3.3. Effect of the doping concentration on absorber and buffer layers

The concentration of acceptor and donor carriers in both the absorber and buffer layers profoundly impacts the efficiency of solar cells. In this simulation study, the impact of changing the concentration of acceptor and donor carriers from 10^{15} cm^{-3} – 10^{20} cm^{-3} on the photovoltaic parameters for both proposed solar cells has been investigated. **Fig. 8** presents contour plots of the efficiency of both proposed solar cells under varying doping concentrations in the absorber and buffer layers. Other parameters, as specified in **Table 1**, have been held constant in this simulation study.

In **Fig. 8** (a), the highest efficiency of the proposed solar cell with the WO_3 buffer layer can be achieved when the density of acceptor carriers

is around $\sim 10^{16} \text{ cm}^{-3}$ and the density of donor carriers is in the range of 10^{18} – 10^{19} cm^{-3} . On the other hand, the relatively high efficiency of the proposed solar cell with the WS_2 buffer layer can be achieved when the density of acceptor carriers is around $\sim 10^{16} \text{ cm}^{-3}$, but at this value of the density of acceptor carriers, variations in the density of donor carriers do not affect the photovoltaic parameters (**Fig. 8** (b)).

To find the optimal density of acceptor carriers in the absorber layer, we have examined the effect of varying the density of acceptor carriers on the solar cell performance. This analysis considers a constant density of donor carriers in the buffer layer at 10^{18} cm^{-3} and keeps all other physical parameters constant as per **Table 1**. The results are shown in **Fig. 9** (a) and (b).

Fig. 9 (a) reveals a consistent behavior in both the V_{oc} and FF parameters in the $\text{Au}/\text{Sb}_2\text{Se}_3/\text{WO}_3/\text{ITO}$ solar cell as the density of acceptor carriers increases from 10^{15} to 10^{18} cm^{-3} . V_{oc} increases from 0.498 to 0.596 V, and FF also experiences an increase from 47.80 % to 57.79 %. Then, FF significantly increases with further increases in the density of acceptor carriers up to 10^{20} cm^{-3} . J_{sc} , within the range of 10^{15} – 10^{16} cm^{-3} , increases from 28.740 to 30.808 mA/cm^2 , and afterward, it decreases with further increases in the density of acceptor carriers, remaining nearly constant. The decrease in J_{sc} is due to the diminishing charge collection region and internal electric field. This makes the movement of generated charge carriers at a greater distance from the junction more difficult, resulting in a decrease in J_{sc} [67]. When the density of acceptor carriers increases from 10^{15} to 10^{16} cm^{-3} , the efficiency improves from 6.83 % to 9.51 %, and after that, further increases in the density of acceptor carriers lead to a decrease in efficiency. **Fig. 9** (b) illustrates a similar behavior for both the V_{oc} and FF parameters in the $\text{Au}/\text{Sb}_2\text{Se}_3/\text{WS}_2/\text{ITO}$ solar cell as the density of acceptor carriers increases. As the density of acceptor carriers increases from 10^{15} to 10^{18} cm^{-3} in the $\text{Au}/\text{Sb}_2\text{Se}_3/\text{WS}_2/\text{ITO}$ solar cell, V_{oc} rises from 0.495 to 0.596 V, and FF increases from 54.52 % to 72.76 %. Then, a significant growth is observed up to the density of acceptor carriers 10^{20} cm^{-3} . J_{sc} increases from 27.556 mA/cm^2 at a density of acceptor carriers 10^{15} cm^{-3} to 29.149 mA/cm^2 at a density of acceptor carriers 10^{16} cm^{-3} , followed by a decrease until the density of acceptor carriers 10^{19} cm^{-3} , and afterward, remains nearly constant. Nevertheless, with an increase in the density of acceptor carriers from 10^{15} to 10^{16} cm^{-3} , η improves from 7.43 % to 9.79 %. Beyond this point, further increases in the density of acceptor carriers result in a decrease in efficiency. Through the analysis of the graphs, the optimal density of acceptor carriers in the absorber layer for both proposed solar cells is selected as 10^{16} cm^{-3} . To determine the optimum density of donor carriers in the buffer layers WO_3 and WS_2 for both proposed solar cells, the simulation results of photovoltaic parameters are presented in **Fig. 10**, by varying the carrier

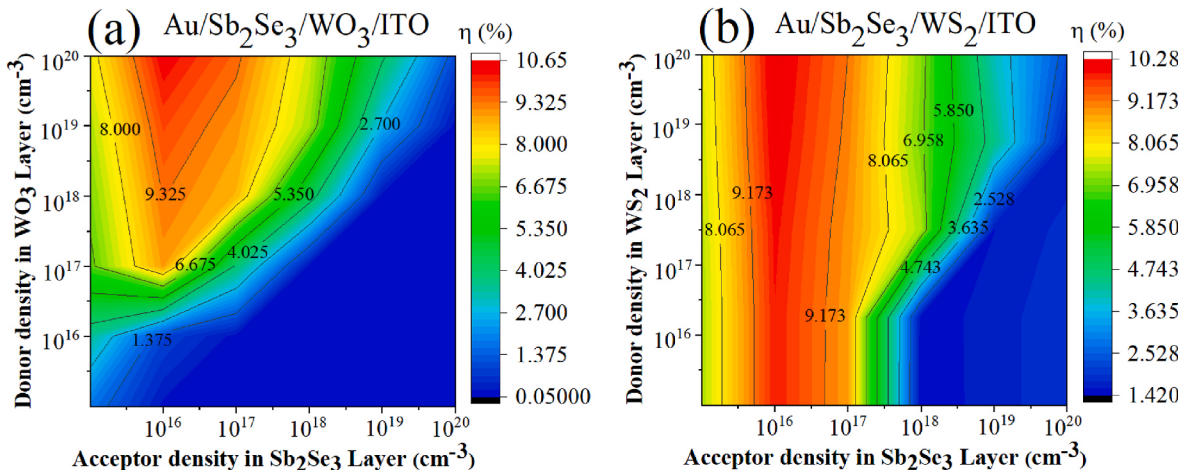


Fig. 8. Contour plots of variation of efficiency with the doping concentration on absorber and buffer layers solar cells (a) $\text{Au}/\text{Sb}_2\text{Se}_3/\text{WO}_3/\text{ITO}$ (b) $\text{Au}/\text{Sb}_2\text{Se}_3/\text{WS}_2/\text{ITO}$.

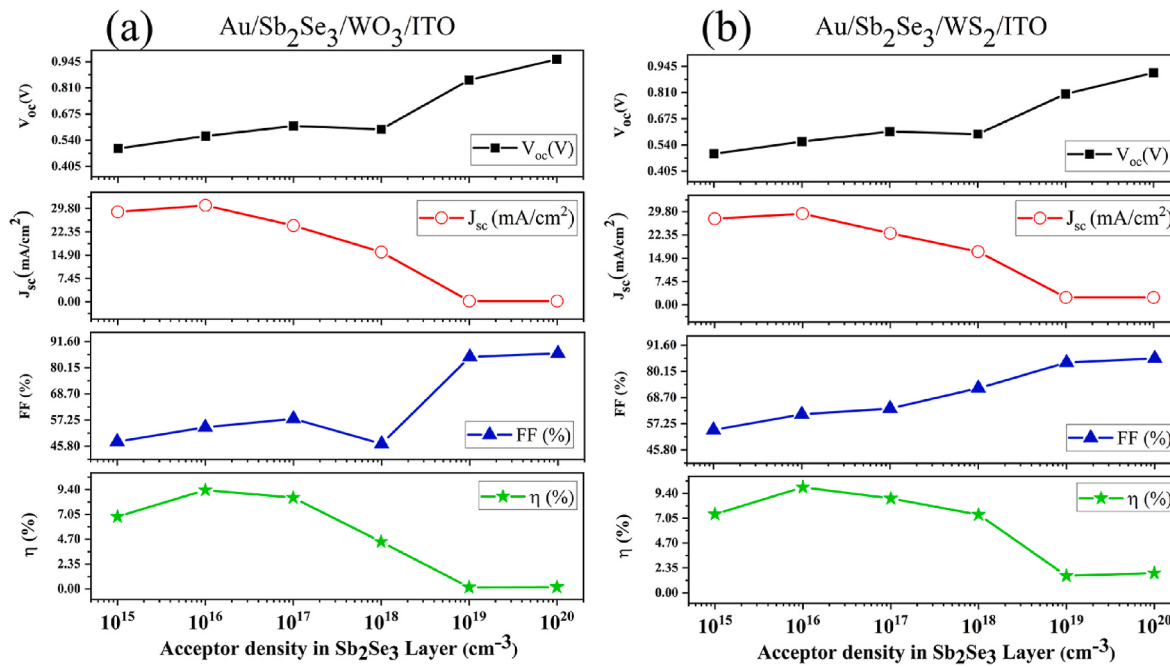


Fig. 9. Output of IV parameters with Sb₂Se₃ acceptor density for (a) Au/Sb₂Se₃/WO₃/ITO and (b) Au/Sb₂Se₃/WS₂/ITO devices.

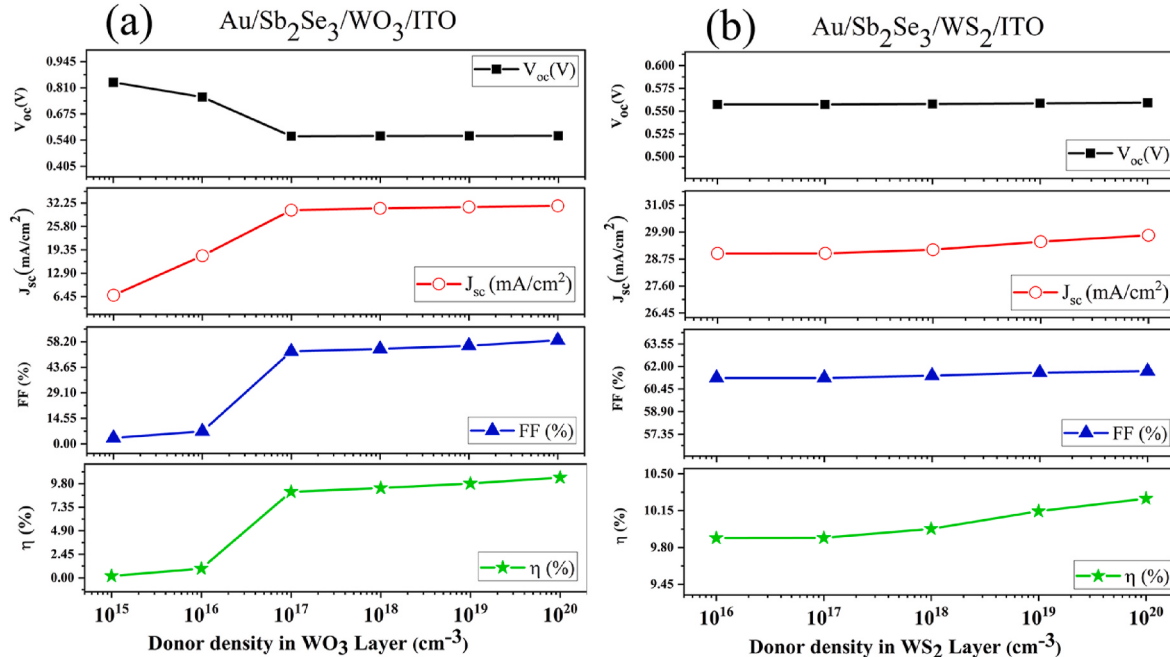


Fig. 10. Output of IV parameters with buffer layer donor density for (a) Au/Sb₂Se₃/WO₃/ITO and (b) Au/Sb₂Se₃/WS₂/ITO devices.

concentrations from 10¹⁵ to 10²⁰ cm⁻³. As seen in Fig. 10 (a), for the solar cell with the WO₃ buffer layer, an increase in the density of carrier donors exhibits similar behavior in two parameters both two parameters, η and FF. Initially, both parameters experienced an increase with a steep slope from a density of 10¹⁵–10²⁰ cm⁻³. Between 10¹⁶ to 10¹⁷ cm⁻³, the increase becomes steeper, and finally, from 10¹⁷ to 10²⁰ cm⁻³, the increase is very slow (almost constant). The J_{sc} parameter also shows a similar behavior, with the difference that it initially has a steeper slope and then increases with a gentler slope. The V_{oc} graph, on the other hand, shows an opposite behavior to these three graphs. Initially, it experiences a steep decrease from a density of 10¹⁵–10¹⁷ cm⁻³, and finally, it remains nearly constant up to a concentration of 10²⁰ cm⁻³. In

Fig. 10 (b), for the solar cell with the WS₂ buffer layer, it is evident that with an increase in the density of carrier donors, all four parameters V_{oc}, J_{sc}, FF, and η show almost similar behavior. As the density of donor carriers changes from 10¹⁵ to 10²⁰ cm⁻³, V_{oc} improves from 0.557 to 0.559 V, J_{sc} decreases from 991.28 to 762.29 mA/cm², FF increases from 61.61 % to 67.61 %, and η improves from 8.90 % to 10.65 %.

3.3.4. The impact of series and shunt resistances on the efficiency of device's

This section explores the impact of series resistance (R_s) and shunt resistance (R_{sh}) on the photovoltaic parameters of both suggested device structures. R_s in a solar cell arise from various sources, including

resistances related to layers, interfaces resistances between layers, and metallic contacts within the solar cell. On the other hand, R_{sh} is related to the inverse saturation current [68]. To enhance the performance of solar cells, R_s must be minimized, and R_{sh} should be maximized to prevent voltage drop at the device connections [69–71]. This change facilitates the improvement of electrical current and the transfer of solar energy to electrons and leads to an increase in the energy efficiency of solar cells.

R_s was changed from 1 to $10 \Omega\text{-cm}^2$ to examine its effect on the performance of both proposed devices. Meanwhile, the R_{sh} was considered constant at $10^6 \Omega\text{-cm}^2$. The alterations in photovoltaic parameters with the change in R_s and also the J-V characteristic curves for both proposed solar cells are shown in Fig. 11. As depicted in Fig. 11 (a), for the solar cell with the Au/Sb₂Se₃/WO₃/ITO structure, V_{oc} remains almost constant despite the increase in series resistance, displaying an independent behavior from R_s . However, J_{sc} gradually decreases from 30.856 to 28.922 mA/cm² as R_s increases from 1 to $10 \Omega\text{-cm}^2$. Also, FF and η follow the same trend, decreasing linearly with the increase in R_s . FF decreases from 55.08 % to 31.73 %, and η decreases from 9.53 % to 5.15 % for R_s of 1 and $10 \Omega\text{-cm}^2$, respectively. Similarly, as shown in Fig. 11 (c), for the Au/Sb₂Se₃/WS₂/ITO solar cell structure, V_{oc} is

independent of the R_s , maintaining an almost constant value with increasing R_s . However, J_{sc} experiences a decrease gently with R_s series resistance from 1 to $10 \Omega\text{-cm}^2$, decreasing from 29.189 to 27.729 mA/cm², respectively. FF and η show a similar decreasing trend with increasing R_s . FF decreases from 62.34 % to 37.64 %, and η decreases from 10.151 % to 5.823 %, respectively, for the same changes in R_s . As observed from Fig. 11 (b) and (d), the J-V characteristic curves for both proposed solar cells change shape with increasing R_s . These results indicate that as R_s increases, the efficiency of the solar cell decreases, which leads to a decrease in the output current of the solar cell.

R_{sh} was changed from 100 to $1 \times 10^9 \Omega\text{-cm}^2$ to study its effect on the performance of both proposed devices while maintaining a constant value of R_s at $1 \Omega\text{-cm}^2$. Fig. 12 shows variations in photovoltaic parameters with the change in R_{sh} , along with the corresponding J-V characteristic curves for both proposed devices. Fig. 12 (a) and (b), respectively, depict the photovoltaic output parameters of the Au/Sb₂Se₃/WO₃/ITO and Au/Sb₂Se₃/WS₂/ITO solar cells as a function of R_{sh} . The simulation results demonstrate a substantial increase in all photovoltaic parameters (V_{oc} , J_{sc} , FF , and η) with an increase in R_{sh} up to $1 \times 10^4 \Omega\text{-cm}^2$. It is further observed that all photovoltaic parameters reach saturation after reaching the value of $1 \times 10^6 \Omega\text{-cm}^2$ and remain

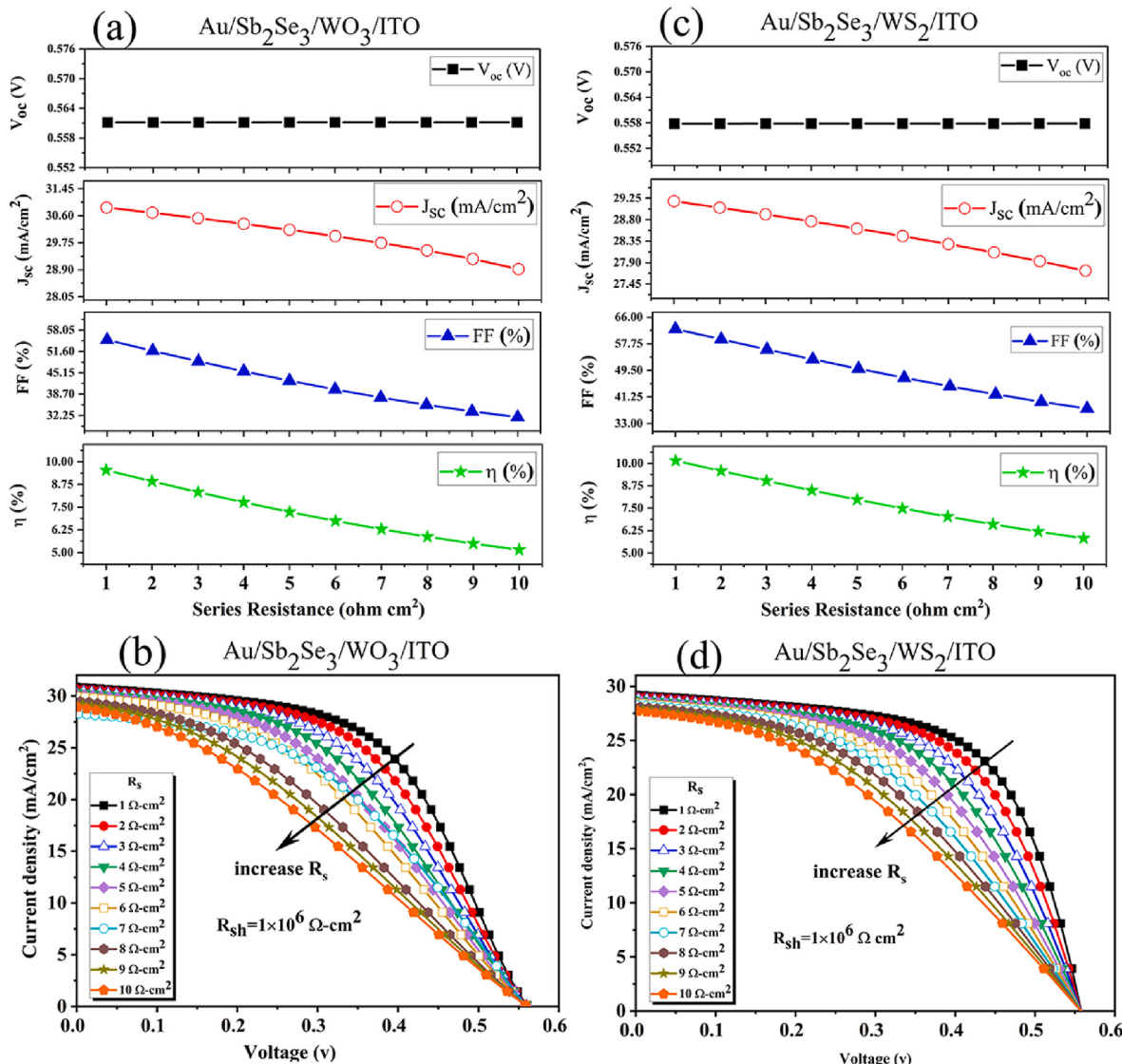


Fig. 11. (a and c) Effect of series resistance on the output of IV parameters for both proposed devices, (b and d) Impact of R_s on the J-V characteristic curve of the proposed solar cells.

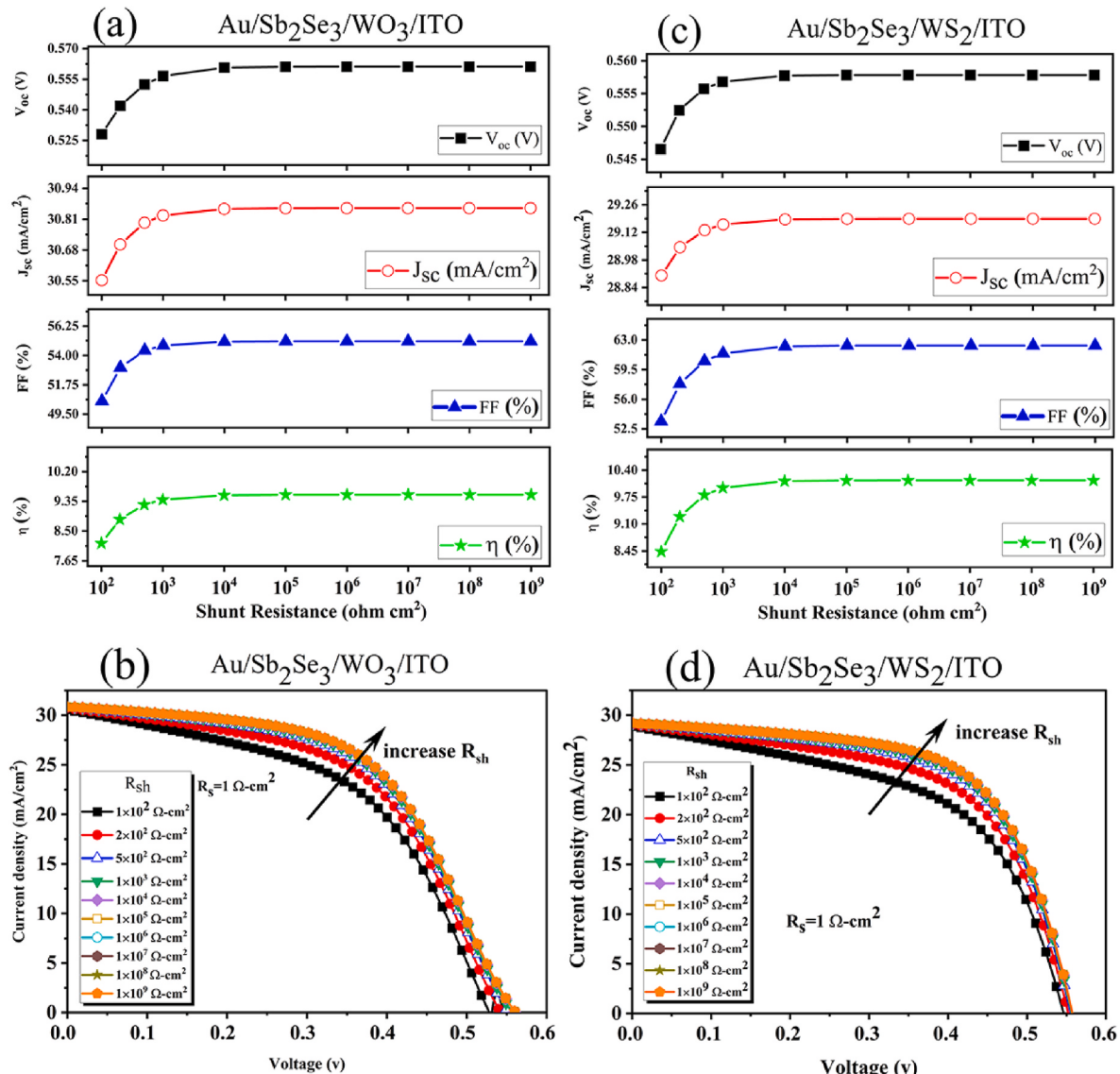


Fig. 12. (a and c) Effect of shunt resistance on the output of IV parameters for both proposed devices, (b and d) Impact of R_{sh} on the J-V characteristic curve of the proposed solar cells.

unchanged. The results obtained follow the same trend as reported in previous studies [45]. As illustrated in Fig. 12 (b) and (d), the variations in the J-V characteristic curves for both proposed solar cells as a function of R_{sh} . The figures and simulation results indicate that a decrease in R_{sh} leads to a reduction in the performance of the solar cell, consequently diminishing the photovoltaic efficiency. Hence, these findings demonstrate that variables such as R_s and R_{sh} wield substantial influence over solar cell performance, emphasizing the need for meticulous consideration in designing and optimizing solar cell devices.

3.3.5. Effect of temperature on solar cell device's performance

The temperature has a main impact on the performance of solar cells and can strongly influence their electrical characteristics. The effect of temperature depends on the type of semiconductor material and the structure of the cell, but in general, it affects the absorption of light, the band gap energy, the carrier density, and the carrier mobility [72,73]. In this section, the influence of temperature on the performance of both proposed solar cells is investigated by varying the operational temperature from 280 K to 420 K. Fig. 13 (a) and (b) show the simulation result of the photovoltaic output parameters of Au/Sb₂Se₃/WO₃/ITO and Au/Sb₂Se₃/WS₂/ITO devices, respectively, as a function of temperature.

Fig. 13 (a) illustrates that for the Au/Sb₂Se₃/WO₃/ITO solar cell structure, V_{oc} decreases linearly from 0.611 V at 280 K to 0.256 V at 420 K with an increase in the cell temperature.

Similarly, as depicted in Fig. 13 (b), for the Au/Sb₂Se₃/WS₂/ITO solar cell structure, V_{oc} decreases linearly from 0.607 V at 280 K to 0.252 V at 420 K with the increase in temperature. According to the Shockley-Queisser relationship, V_{oc} depends on both J_{sc} and J_0 , which is expressed by Eq. (4) [74,75].

$$V_{oc} = \frac{kT}{e} \ln \left[\frac{J_{sc}}{J_0} + 1 \right] \quad (4)$$

Where T, k, e, J_{sc} , and J_0 represent temperature, Boltzmann constant, elementary charge, short-circuit current density, and reverse saturation current density, respectively. Indeed, an increase in temperature leads to an increase in the reverse saturation current density (J_0) in the solar cell. The rising J_0 contributes to enhanced carrier recombination within the solar cell. As a result, with increasing carrier recombination, V_{oc} decreases, and this change leads to the degradation of solar cell efficiency at high temperatures. The simulation results presented in Fig. 13 (a) show that for the Au/Sb₂Se₃/WO₃/ITO solar cell, J_{sc} experiences a slight increase with rising temperature until 320 K, reaching a maximum value

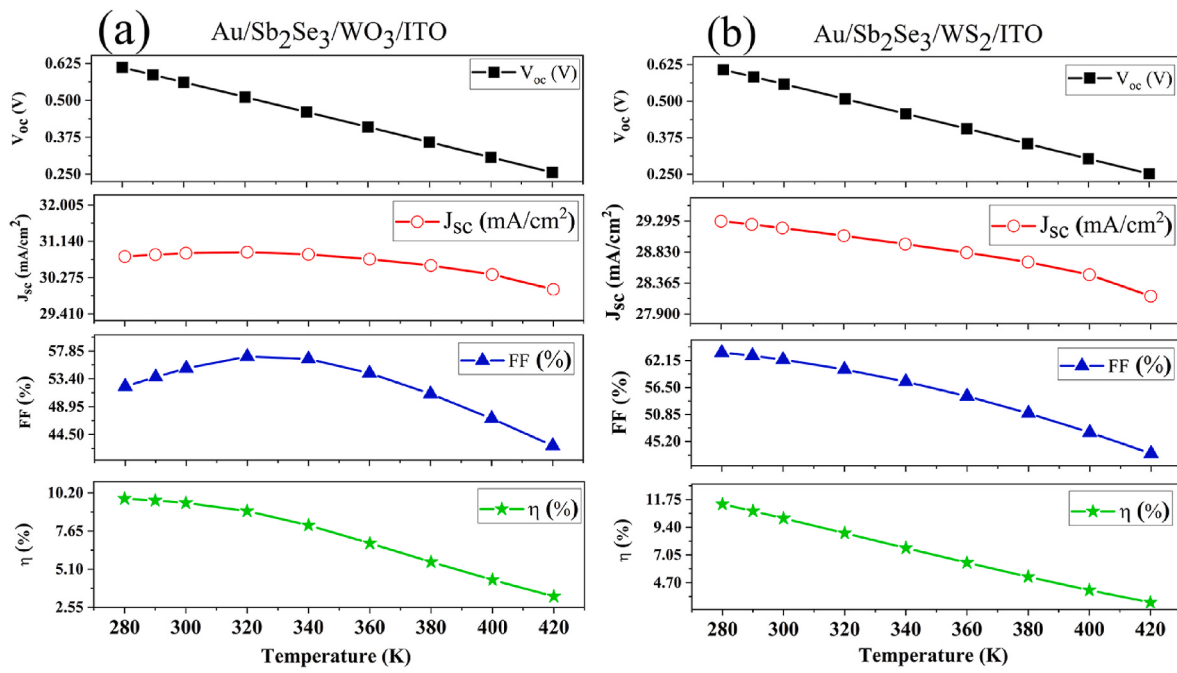


Fig. 13. Effect of operating temperature on the output of IV parameters for (a) Au/Sb₂Se₃/WO₃/ITO and (b) Au/Sb₂Se₃/WS₂/ITO devices.

of 30.856 mA/cm², after which it gradually decreases. The energy conversion efficiency of the solar cell declines from 9.818 % at 280 K to 3.279 % at 420 K. Similarly, it is observed from Fig. 13 (b) that for the Au/Sb₂Se₃/WS₂/ITO solar cell, J_{sc} gradually decreases from 29.229 mA/cm² at 280 K to 28.168 mA/cm² at 420 K. It is found from the simulation results that the energy conversion efficiency of the Au/Sb₂Se₃/WS₂/ITO solar cell decreases from 11.357 % at 280 K to 3.027 % at 420 K. The increase in temperature will lead to an increase in J_0 in the solar cell for two reasons: Firstly, as the temperature increases, more electron-hole pairs are generated in the p-n junction of the solar cell, leading to an increase in minority carriers [76]. Secondly, the bandgap is directly influenced by temperature [77]. With the temperature rise, the bandgap of semiconductor materials becomes narrower, allowing minority carriers to overcome the energy barrier more easily and leading to increased carrier recombination in the solar cell [78,79]. As recombination increases due to the higher J_0 , fewer free carriers are available for the current generation. Consequently, the V_{oc} of the solar cell decreases, affecting its overall efficiency [80]. The lower efficiency of solar cells at higher temperatures is attributed to the temperature dependence of various factors, including carrier concentration, electron and hole mobility, and energy bandgaps of materials. This behavior is consistent with and aligns well with the results reported in previous studies [23, 73].

3.3.6. Study of activation energy

Activation energy (E_a) is a critical parameter that holds significant importance in the performance of TFSCs. The presence of recombination centers at the absorber/buffer interface and the charge depletion region has been identified as having a significantly negative impact on the efficiency of TFSCs. These recombination centers typically form due to lattice mismatch and energy level misalignment between the layers. One effective method to characterize the presence of these recombination centers is to obtain the activation energy [81]. The dependence of V_{oc} on temperature (V_{oc} -T) is employed to estimate the activation energy in the absorber/buffer interface, as presented in Eq. (5) [61,82].

$$V_{oc} = \frac{E_a}{q} - \frac{AkT}{q} \ln\left(\frac{J_{00}}{J_L}\right) \quad (5)$$

Where q, E_a , k, T, A, J_L , and J_{00} represent the elementary charge,

activation energy for recombination, Boltzmann constant, temperature, ideality factor, light current density, and reverse saturation current, respectively. In Eq. (5), assuming A, J_{00} , and J_L are independent of temperature and considering a linear relationship between V_{oc} and T, extrapolating the V_{oc} -T curve allows us to calculate the E_a at T = 0 K [83].

Recombination in TFSCs takes place in different locations because the charge carriers are generated in different regions, including the space charge region (SCR), the front, the bulk, and the back of the solar cell. The charge carriers generated near the SCR, or depleted region, are separated by the electric field of the SCR. However, the charge carriers generated on the front, bulk, and back of the solar cell are less likely to be separated. In TFSCs, there are three main types of recombination losses that affect the performance of the solar cell, namely: 1) recombination losses in the bulk; 2) recombination losses at the interface; and 3) recombination losses in the contact [84]. The predominant losses in TFSCs can be evaluated using the activation energy of recombination (E_a). A model has been proposed that accounts for recombination losses due to Shockley-Read-Hall (SRH) recombination [36,85]. Previous studies have discussed that when $E_a < E_g, \text{Absorber}$, the primary recombination mechanism in solar cells is usually interfacial recombination between the absorber/buffer layers. However, when $E_a = E_g, \text{Absorber}$ or $E_a > E_g, \text{Absorber}$, the primary recombination mechanism in solar cells tends to be Shockley-Read-Hall (SRH) recombination within the space charge region (SCR), which dominates over recombination at the interface. Interfacial recombination in TFSCs occurs when electrons and holes recombine at the interfaces between different layers in the device. Several factors, such as defects, energy level mismatches, and imperfect interface structures, lead to the creation of localized recombination sites, which impair the efficiency of the solar cell. Recombination in the space charge region in TFSCs occurs because charge carriers recombine within this region of the device. The SCR is formed due to differences in doping concentrations, band alignment, and defect states within the bandgap, which act as trap sites between adjacent layers. Consequently, this phenomenon causes charge carriers to recombine before they can contribute to the photocurrent [82,86,87]. In this section, we estimated the main recombination effect by finding E_a for both proposed solar cell structures with WO₃ and WS₂ buffer materials, as well as the absorber (Sb₂Se₃). The V_{oc} -T characteristics for both proposed solar cell

structures, namely Au/Sb₂Se₃/WO₃/ITO and Au/Sb₂Se₃/WS₂/ITO, are shown in Fig. 14, allowing for the determination of the activation energy. Fig. 14 demonstrates that E_a, extracted from the plot of V_{oc} versus T at 0 K, is 1.3373 eV and 1.3351 eV for WO₃ and WS₂ ETLs, respectively, which is ~0.14 eV larger than band gap of the absorber layer (E_g = 1.19 eV). Since E_a is greater than E_g of the absorber layer in both proposed solar cells, their recombination process is dominated by SRH recombination in the space charge region, leading to an increased recombination of minority carriers that generated by the defect states within the band gap and, consequently, a decrease in V_{oc} with increasing temperature [41,88,89].

Fig. 15 shows the recombination current densities for Shockley-Read-Hall (SRH), radiation, Auger, and interfacial mechanisms for both proposed solar cells. It can be seen from Fig. 15 that the recombination current density for SRH (J_{SRH}) increases significantly compared to the other recombination current densities. Therefore, based on the J_{SRH} -V curve and considering E_a greater than E_g of the absorber layer, it can be concluded that in both proposed devices, the dominant recombination is of SRH type in the space charge region (SCR) of the absorber layer.

3.3.7. Effect of the work function of the back contact on the device's performance

In a solar cell, the work function of the back contact metal (Φ_m) determines whether holes are easily transferred to the electrode. This parameter signifies the energy required for the transfer of holes from the semiconductor's absorbing layer to the electrode. If the work function is high, the transfer of holes to the electrode is easy. However, if the work function of the metal is low, the transfer of holes is more difficult, and some of them may recombine, which leads to a reduction in the efficiency of the device [90]. For the design of efficient solar cells, the selection of the back contact material and optimization of its work function is essential. This ensures that a suitable ohmic contact is formed between the absorber layer and the back contact, which improves the performance of the cell. In the present simulation study, the work function of the back contact was changed to the range of 4.5 eV–5.6 eV to study its impact on the performance of both proposed devices. Fig. 16 illustrates the variations in the I-V parameters of both proposed devices as a function of Φ_m . It is evident from Fig. 16 that V_{oc}, J_{sc}, FF, and η for both proposed solar cells show an increase in the range of 4.5 eV–5.1 eV. After that, the photovoltaic parameters of the solar cell remain constant and unchanged. In the solar cells Au/Sb₂Se₃/WO₃/ITO and Au/Sb₂Se₃/WS₂/ITO, respectively, η reaches its maximum value, 9.538 %, and 10.151 % at a back electrode work function of 5.1 eV. This suggests that

noble metals such as Au (5.1 eV) [91], Ni (5.5 eV) [91], and Pt (5.6 eV) [92,93], with a work function greater than 5.1 eV, can be used as back contacts (anode electrodes) for efficient charge collection in Sb₂Se₃-based solar cells.

Furthermore, the Schottky barrier height (Φ_b) between the back contact and the absorber layer with bandgap energy (E_{g,absorber}), electron affinity ($\chi_{absorber}$) absorber layer, and φ_m for the majority of carriers can be expressed as follows [35,94]:

$$\Phi_b = E_g \text{ Absorber} - (\Phi_m - \chi_{Absorber}) \quad (6)$$

According to Eq. (6), we can see an increase in the work function from 4.5 eV to 5.6 eV, leading to a reduction in Φ_b from 0.9 eV to –0.2 eV, consequently enhancing the output photovoltaic parameters of the solar cells. Thus, increasing the ohmic resistance at the absorber/back contact (anode) interface leads to an improvement in FF and η . Previous studies have also reported improved performance of solar cells with higher back-contact (anode) work functions [35].

3.3.8. Capacitance-voltage (C-V) characteristic of the solar cell

The Capacitance-Voltage (C-V) characteristic curve in a solar cell reflects the electrical capacitance behavior of the cell in response to voltage changes. This curve is commonly used as a tool to examine and analyze the electrical characteristics of the cell and how they change with voltage. Interpretation of this curve can provide us with a better understanding of the electrical performance of the solar cell under various conditions and its specific features. Parameters such as the depletion region width, majority carrier density, and junction potential can be extracted using this curve. The electrical capacitance of the depletion region is defined by the following relationship [38,95]:

$$C = \frac{dQ}{dV} = \sqrt{\frac{q\epsilon_0\epsilon_s A^2 N}{2(V_{bi} - V)}} = \frac{\epsilon_s}{W} \quad (7)$$

Where C is the capacitance, A is the cross-sectional area of the junction (1 cm²), q is the elementary charge (1.6×10^{-19} C), ϵ_s is the dielectric constant of the semiconductor (according to the input parameter table), ϵ_0 is the permittivity of free space (8.85×10^{-14} F cm⁻¹), N is the carrier density (cm⁻³) representing the concentration of both holes and electrons, V_{bi} is the built-in potential, and V is the applied potential. The built-in potential (V_{bi}) in a p-n junction represents the voltage variation across the junction within a semiconductor device caused by creating a depletion region. Fig. 17 (a) presents the Capacitance-Voltage (C-V) characteristic curve for both proposed solar cell structures. The Mott-Schottky (1/C² vs. V) plot is a crucial analytical

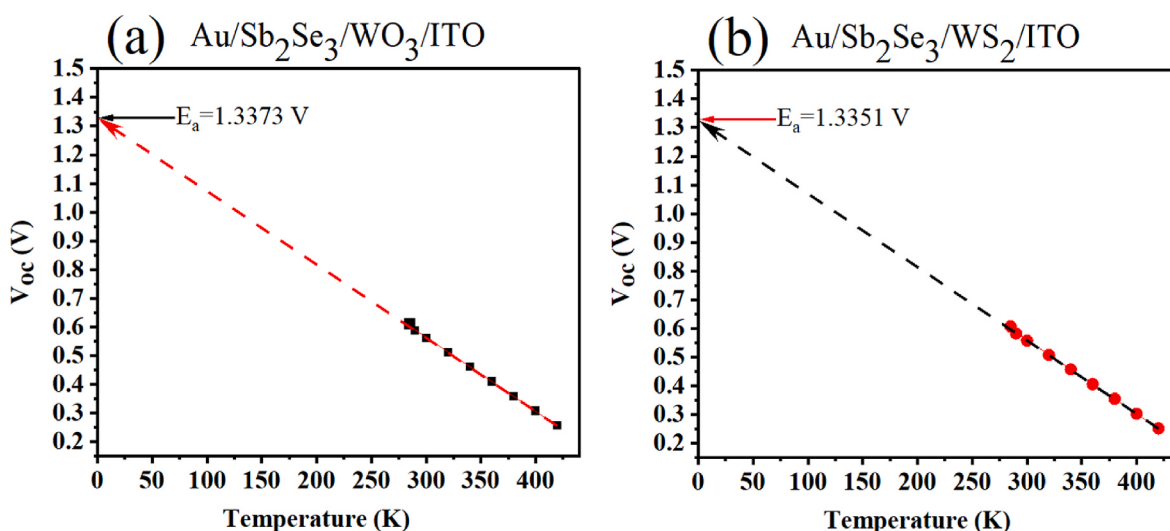


Fig. 14. Estimation of the activation energy (E_a) at the absorber/buffer interface for (a) Au/Sb₂Se₃/WO₃/ITO and (b) Au/Sb₂Se₃/WS₂/ITO devices.

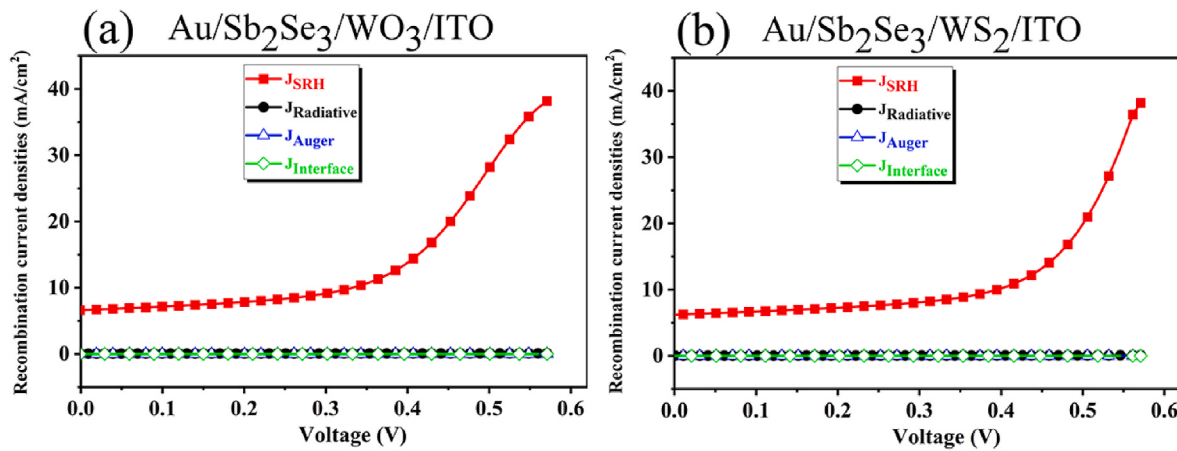


Fig. 15. The current densities of the recombination mechanisms (SRH, radiative, Auger, and interfaces) for (a) Au/Sb₂Se₃/WO₃/ITO and (b) Au/Sb₂Se₃/WS₂/ITO devices.

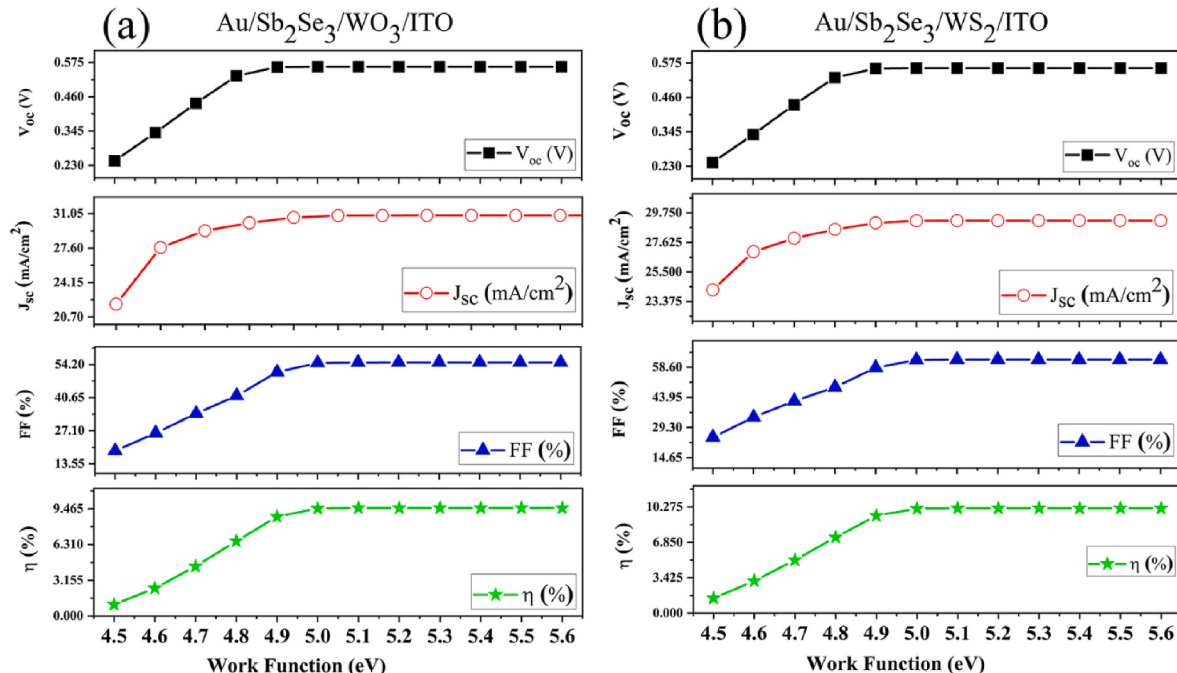


Fig. 16. Effect of the back contact work function on photovoltaic parameters (V_{oc} , J_{sc} , FF, and η) for (a) Au/Sb₂Se₃/WO₃/ITO and (b) Au/Sb₂Se₃/WS₂/ITO devices.

tool used to investigate and analyze electrical properties, including the built-in potential and carrier density, in semiconductor materials and junctions. The formula used to extract these parameters is as follows [38, 95, 96]:

$$\frac{1}{C^2} = \frac{2(V_{bi} - V)}{q\epsilon_0\epsilon_s A^2 N} \quad (8)$$

In the Mott-Schottky curve, the point obtained from the extension of the straight-line slope in the forward bias region on the potential axis is the built-in potential (V_{bi}). As observed in Fig. 17 (b) and (c), the values of $V_{bi} = 0.706$ V and 0.754 V are estimated for the solar cell Au/Sb₂Se₃/WO₃/ITO and Au/Sb₂Se₃/WS₂/ITO, respectively.

3.4. Comparison of the suggested devices with WO₃ and WS₂ buffer layers

For both suggested Sb₂Se₃-based solar cell structures, the absorber layer's optimal thickness and carrier concentration were determined to be 1 μm and 10¹⁶ cm⁻³, respectively. The optimal thickness values for

the WO₃ and WS₂ buffer layers were found to be 0.1 μm and 0.05 μm, respectively, with carrier concentration of 1 × 10¹⁸ cm⁻³ for both. Additionally, at T = 300 K, R_s = 1 Ω·cm², R_{sh} = 10⁶ Ω·cm², and Au as the back metal contact was identified as the optimal parameter values for this numerical simulation. After optimization, the final parameter values in this simulation study for the proposed solar cells are presented in Table 5.

The J-V characteristic curve and EQE of both simulated heterojunction solar cell structures with WO₃ and WS₂ buffer layers are illustrated in Fig. 18, and the output parameters of the solar cell performance for both structures are listed in Table 6. Notably, the replacement of CdS with either WO₃ or WS₂ buffer materials significantly improves the electrical performance parameters of the solar cell structures with Au/Sb₂Se₃/WO₃/ITO and Au/Sb₂Se₃/WS₂/ITO. As evident in Table 6, the proposed solar cells simulated based on WO₃ and WS₂ buffer layers exhibit higher open-circuit voltage and efficiency compared to the CdS-based cells buffer layer. Additionally, WO₃ and WS₂, besides being non-toxic, have an optimal bandgap, making them suitable for the buffer

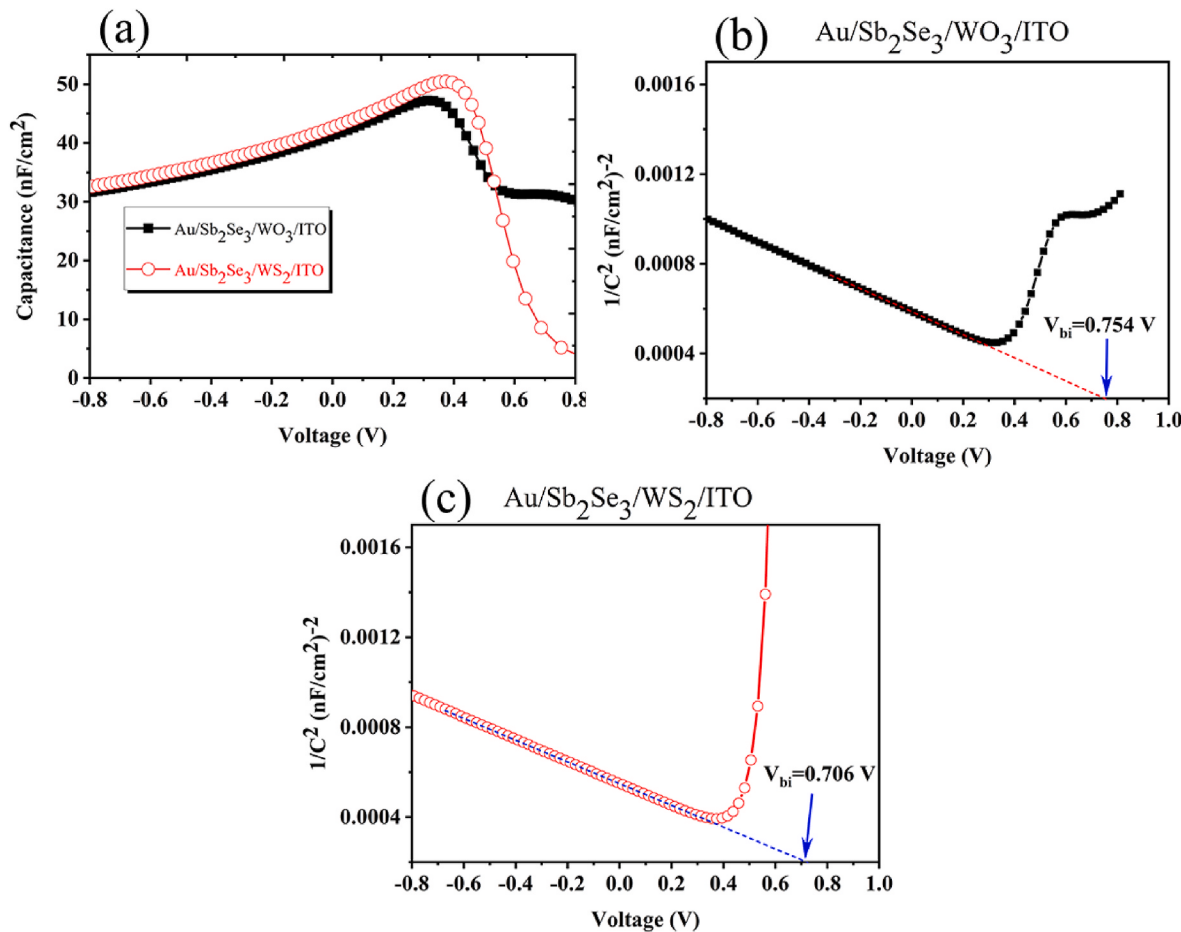


Fig. 17. (a) Variation of Capacitance vs. Voltage, (b) and (c) Mott-Schottky ($1/C^2$ vs. V) plot for Au/Sb₂Se₃/WO₃/ITO and Au/Sb₂Se₃/WS₂/ITO devices.

Table 5

Optimized values of the various parameters of the proposed solar cells in this simulation study.

Optimized parameter (unit)	Solar cell with configuration Au/Sb ₂ Se ₃ /WO ₃ /ITO	Solar cell with configuration Au/Sb ₂ Se ₃ /WS ₂ /ITO
Absorber thickness (μm)	1.0	1.0
Buffer thickness (μm)	0.100	0.05
Donor doping N_D (cm^{-3})	1.0×10^{16}	1.0×10^{16}
Acceptor doping N_A (cm^{-3})	1.0×10^{18}	1.0×10^{18}
R_s ($\Omega \cdot \text{cm}^2$)	1.0	1.0
R_{sh} ($\Omega \cdot \text{cm}^2$)	1.0×10^6	1.0×10^6
Temperature (K)	300	300
Activation energy (eV)	1.3373	1.3351
Work function of the back contact (eV)	5.1	5.1
built-in potential (V_{bi}) (V)	0.706	0.754

layer. This numerical study indicates that these buffer materials can not only match the performance of conventional CdS but also serve as suitable alternatives, as they have higher power conversion efficiency. Since these materials are less reported, they should receive more attention and further experimental and numerical studies are needed to enhance their efficiency.

Finally, Table 7 presents the PV performance parameters obtained from some experimental and simulation results of Sb₂Se₃-based solar cells compared to current work results. Some of these studies are related

to the design of conventional cells, some to structures without HTL, and others to structures based on HTL. It is important to note that HTL-free structures have a lower efficiency than HTL-based solar cells. In previous computational and experimental works, WO₃ and WS₂ have seldom been studied as buffer layers. In experimental studies reported in Table 7, the efficiency of Sb₂Se₃-based solar cells has stayed within 9.2 %, and they also exhibit relatively low V_{oc} values. However, theoretical studies in Table 7 showed that solar cells without HTL and with CdS buffer layers worked better than experimental devices despite having lower V_{oc} values. In our proposed solar cells with structures without an HTL layer, both PCE and V_{oc} have improved, primarily due to optimizing the physical parameters of WO₃ and WS₂ buffer layers. Besides being non-toxic, WO₃ and WS₂ also possess optimal bandgaps, making them highly suitable for buffer layers. This research shows that these buffer materials can not only match the performance of regular CdS devices but can also be used instead of harmful CdS because our suggested devices have better V_{oc} , J_{sc} , and PCE. In particular, the performance of the simulated structures Au/Sb₂Se₃/WO₃/ITO and Au/Sb₂Se₃/WS₂/ITO has increased from 7.580 % to 9.538 % and 10.151 %, respectively. PCE, our proposed solar cell improvement is about 26 % and 34 %, respectively, compared to the conventional Au/Sb₂Se₃/CdS/ITO structure. The absence of CdS makes our device environmentally friendly, and using all-inorganic charge transport layers enhances its environmental stability. Furthermore, abundant and low-cost materials like WO₃ and WS₂ can reduce costs. Overall, our proposed solar cells' promising and innovative performance with WO₃ and WS₂ buffer layers presents a favorable outlook for research and practical applications in thin-film Sb₂Se₃-based PV devices.

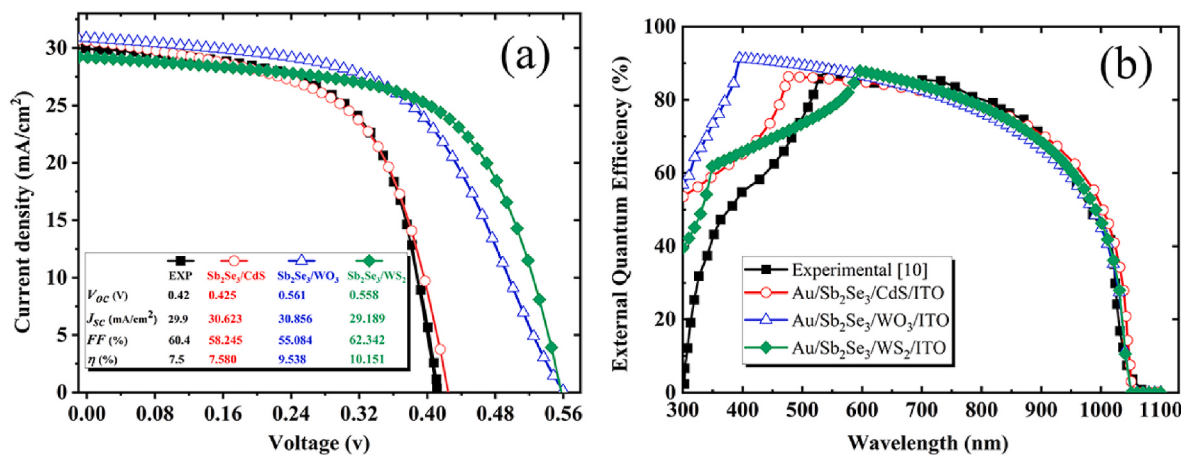


Fig. 18. Comparison of (a) J-V characteristic curve and (b) the external quantum efficiency of experimental, conventional and proposed solar cells in this simulation study.

Table 6

Comparison of the values of the electrical output parameters of the proposed devices in this simulation study.

Solar cell configuration	Electrical parameters			
	V _{oc} (V)	J _{sc} (mA/cm ²)	FF (%)	η (%)
Au/Sb ₂ Se ₃ /CdS/ITO (Reference)	0.425	30.623	58.245	7.580
Au/Sb ₂ Se ₃ /WO ₃ /ITO	0.561	30.856	55.084	9.538
Au/Sb ₂ Se ₃ /WS ₂ /ITO	0.558	29.189	62.342	10.151

4. Conclusions

In summary, this numerical study focused on TFSc based on Sb₂Se₃ with WO₃ and WS₂ buffer layers, modeled and studied as ETL utilizing SCAPS-1D software. Initially, the conventional Sb₂Se₃ solar cell's (Au/Sb₂Se₃/CdS/ITO) performance was compared with experimental data. Subsequently, the proposed structures of Au/Sb₂Se₃/WO₃/ITO and Au/Sb₂Se₃/WS₂/ITO were modeled and investigated. The suggested Sb₂Se₃-based solar cells with WO₃ and WS₂ buffer layers showed higher efficiency at a defect density of $1 \times 10^{15} \text{ cm}^{-3}$ in the absorber layer compared to conventional CdS-layered solar cells. The impact of the thickness and carrier concentration in the absorber and buffer layers on the performance of the solar cell was investigated to determine the optimal parameters. Both structures exhibit high performance at low thickness values of absorber and buffer layers (absorber thickness of 1 μm, 0.1 μm for WO₃, and 0.05 μm for WS₂). For both proposed solar cells, the CBO is positive (Spike-like) in the absorber/buffer interface. The CBO values for structures with the WO₃ and WS₂ buffer layers are 0.38 eV and 0.23 eV, respectively. The optimal concentration of charge carrier density in the absorber layer is chosen to be $1 \times 10^{16} \text{ cm}^{-3}$ for both structures. As well as the optimal concentration of charge carrier density for both WO₃ and WS₂ buffer layers is selected to be $1 \times 10^{18} \text{ cm}^{-3}$. By varying the operational temperature, R_s, R_{sh}, and Φ_m, the electrical parameters of the proposed devices have been investigated and optimized. Using these optimized values, the results of the electrical parameters obtained in this simulation study for Au/Sb₂Se₃/WO₃/ITO cell configuration were determined to η = 9.538 %, V_{oc} = 0.561 V, J_{sc} = 30.856 mA/cm², and FF = 55.084 %. Additionally, we observed enhancements in the PCE with values of η = 10.151 %, V_{oc} = 0.558 V, J_{sc} = 29.189 mA/cm², and FF = 62.342 % for the Au/Sb₂Se₃/WS₂/ITO structure. Finally, the activation energy and the capacitance-voltage (C-V) characteristics were investigated for both proposed devices. The activation energy values of 1.3373 eV and 1.3351 eV and the V_{bi} values of 0.754 V and 0.706 V are estimated for solar cells with buffer layers WO₃ and WS₂, respectively.

Table 7

Comparison of electrical parameters of the Sb₂Se₃ TFSCs in the previous studies and this work.

Research type	Solar cell configuration	Electrical parameters				Ref.
		V _{oc} (V)	J _{sc} (mA/cm ²)	FF (%)	PCE (%)	
Exp.	Au/Sb ₂ Se ₃ /CdS/ITO	0.42	29.90	60.40	7.6	[10]
	Au/Sb ₂ Se ₃ /CdS/FTO	0.33	27.69	45.04	4.77	[97]
	Au/Sb ₂ Se ₃ /TiO ₂ /FTO	0.45	25.44	48.96	5.48	[98]
	Au/Sb ₂ Se ₃ /ZnO/FTO	0.32	26.6	43.5	3.92	[99]
	Mo/Sb ₂ Se ₃ /TiO ₂ /CdS/FTO	0.40	35.58	70.3	9.2	[11]
	Au/CuSCN (HTL)/Sb ₂ Se ₃ /CdS/ITO	0.41	30.51	58.99	7.5	[100]
	Au/PbS (HTL)/Sb ₂ Se ₃ /CdS/ITO	0.42	25.5	59.3	6.5	[9]
	Au/Sb ₂ Se ₃ /CdS/FTO	0.50	32.58	63.10	10.37	[15]
	Au/Sb ₂ Se ₃ /CdS/FTO	0.41	38.15	74.08	11.52	[13]
	Mo/Sb ₂ Se ₃ /ZnO:Al:ZnO	0.36	34.07	67.1	8.26	[32]
	Mo/Sb ₂ Se ₃ /ZnMgO:Al:ZnO	0.53	34.89	74.45	13.97	[32]
	Mo/Sb ₂ Se ₃ /CdS/ZnO:Al:ZnO	0.40	32.56	70.3	9.17	[32]
	Au/CuO (HTL)/Sb ₂ Se ₃ /CdS/ITO	0.64	33.54	74.43	16.06	[15]
	CNT/Cu ₂ O (HTL)/Sb ₂ Se ₃ /In ₂ S ₃ /ITO	0.67	26.84	79.74	13.20	[21]
Theo.	Au/Sb ₂ Se ₃ /WO ₃ /ITO	0.38	30.37	58.09	6.76	[35]
	Au/Sb ₂ Se ₃ /WS ₂ /FTO	0.38	28.18	58.53	6.28	[35]
	Au/Sb ₂ Se ₃ /CdZnS/FTO	0.38	31.60	58.48	7.13	[35]
	Mo/MoSe ₂ /Sb ₂ Se ₃ (SnO ₂ -CdZnS)/FTO	0.66	34.37	82.78	18.77	[35]
	Au/Sb ₂ Se ₃ /WO ₃ /ITO	0.561	30.856	55.084	9.538	This work
	Au/Sb ₂ Se ₃ /WS ₂ /ITO	0.558	29.189	62.342	10.151	This work

To be published in: **Solar Energy Materials and Solar Cells.**

CRediT authorship contribution statement

Khulood Jamal Abbas: Methodology, Investigation, Formal analysis, Data curation. **Amir Bahrami:** Writing – review & editing, Writing – original draft, Validation, Project administration, Methodology, Investigation, Formal analysis.

Declaration of competing interest

The authors declare that they have no recognized financial interests or personal relationships that could be perceived to influence the work reported in this paper.

Data availability

Data will be made available on request.

Acknowledgment

The authors of the Ahvaz Branch, Islamic Azad University, Ahvaz, Iran appreciate their support for this research work. The authors also would like to thank Prof. Burgelman and his colleagues at the University of Gent, Belgium, for sharing the SCAPS software and the opportunity to use it in this research.

References

- [1] S. Chowdhury, A.S. Najm, M. Luengchavanon, A.M. Holi, C.H. Chia, k. Techato, S. Channumsin, I.K. Salih, Investigating the effect of nonideal conditions on the performance of a planar Sb2Se3-based solar cell through SCAPS-1D simulation, *Energies* 37 (2023) 6722–6732.
- [2] A. Mavlonov, T. Razykov, F. Raziq, J. Gan, J. Chantana, Y. Kawano, T. Nishimura, H. Wei, A. Zakutayev, T. Minemoto, X. Zu, S. Li, L. Qiao, A review of Sb2Se3 photovoltaic absorber materials and thin-film solar cells, *Sol. Energy* 201 (2020) 227–246.
- [3] M. Okil, A. Shaker, I.S. Ahmed, T.M. Abdolkader, M.S. Salem, Design and analysis of Sb2S3/Si thin film tandem solar cell, *Sol. Energy Mater. Sol. Cells* 253 (2023).
- [4] T.I. Alanazi, A. Alanazi, E. Touti, A.M. Agwa, H. Kraiem, M. Alanazi, A. M. Alanazi, M. El Sabbagh, Proposal and numerical analysis of organic/Sb2Se3 all-thin-film tandem solar cell, *Polymers* 15 (2023).
- [5] S. Messina, M.T.S. Nair, P.K. Nair, Antimony sulfide thin films in chemically deposited thin film photovoltaic cells, *Thin Solid Films* 515 (2007) 5777–5782.
- [6] Y. Zhou, M. Leng, Z. Xia, J. Zhong, H. Song, X. Liu, B. Yang, J. Zhang, J. Chen, K. Zhou, J. Han, Y. Cheng, J. Tang, Solution-Processed antimony selenide heterojunction solar cells, *Adv. Energy Mater.* 4 (2014).
- [7] Y.C. Choi, T.N. Mandal, W.S. Yang, Y.H. Lee, S.H. Im, J.H. Noh, S.I. Seok, Sb2Se3-sensitized inorganic-organic heterojunction solar cells fabricated using a single-source precursor, *Angew. Chem.* 126 (2014) 1353–1357.
- [8] L. Wang, D.-B. Li, K. Li, C. Chen, H.-X. Deng, L. Gao, Y. Zhao, F. Jiang, L. Li, F. Huang, Y. He, H. Song, G. Niu, J. Tang, Stable 6%-efficient Sb2Se3 solar cells with a ZnO buffer layer, *Nat. Energy* 2 (2017).
- [9] C. Chen, L. Wang, L. Gao, D. Nam, D. Li, K. Li, Y. Zhao, C. Ge, H. Cheong, H. Liu, 6.5% certified efficiency Sb2Se3 solar cells using PbS colloidal quantum dot film as hole-transporting layer, *ACS Energy Lett.* 2 (2017) 2125–2132.
- [10] X. Wen, C. Chen, S. Lu, K. Li, R. Kondrotas, Y. Zhao, W. Chen, L. Gao, C. Wang, J. Zhang, Vapor transport deposition of antimony selenide thin film solar cells with 7.6% efficiency, *Nat. Commun.* 9 (2018) 1–10.
- [11] Z. Li, X. Liang, G. Li, H. Liu, H. Zhang, J. Guo, J. Chen, K. Shen, X. San, W. Yu, 9.2%-efficient core-shell structured antimony selenide nanorod array solar cells, *Nat. Commun.* 10 (2019) 125.
- [12] W. Shockley, H.J. Queisser, Detailed balance limit of efficiency of p-n junction solar cells, *J. Appl. Phys.* 32 (1961) 510.
- [13] L.-y. Lin, L.-q. Jiang, Y. Qiu, B.-d. Fan, Analysis of Sb2Se3/CdS based photovoltaic cell: a numerical simulation approach, *J. Phys. Chem. Solid.* 122 (2018) .19–24.
- [14] F. Baig, Y.H. Khattak, B.M. Soucase, S. Beg, S.R. Gillani, S. Ahmed, A Baseline for the numerical study of Sb2Se3 absorber material based solar cell, *J. Nanoelectron. Optoelectron.* 14 (2019) 72–79.
- [15] Z.-Q. Li, M. Ni, X.-D. Feng, Simulation of the Sb2Se3 solar cell with a hole transport layer, *Mater. Res. Express* 7 (2020) 16416.
- [16] B.K. Mondal, S.K. Mostaque, J. Hossain, Theoretical insights into a high-efficiency Sb2Se3-based dual-heterojunction solar cell, *Heliyon* 8 (2022) e09120.
- [17] Mamta, K.K. Maurya, V.N. Singh, Efficient Sb2Se3 solar cell with a higher fill factor: a theoretical approach based on thickness and temperature, *Sol. Energy* 230 (2021) 803–809.
- [18] R. Kumari, M. Mamta, R. Kumar, Y. Singh, V.N. Singh, 24% efficient, simple ZnSe/Sb2Se3 heterojunction solar cell: an analysis of PV characteristics and defects, *ACS Omega* 8 (2022) 1632–1642.
- [19] S.R. Al Ahmed, A. Sunny, S. Rahman, Performance enhancement of Sb2Se3 solar cell using a back surface field layer: a numerical simulation approach, *Sol. Energy Mater. Sol. Cells* 221 (2021) 110919.
- [20] A. Basak, U.P. Singh, Numerical modelling and analysis of earth abundant Sb2S3 and Sb2Se3 based solar cells using SCAPS-1D, *Sol. Energy Mater. Sol. Cells* 230 (2021) 111184.
- [21] F. Baig, Y.H. Khattak, S. Beg, B.M. Soucase, Numerical analysis of a novel CNT/Cu2O/Sb2Se3/In2S3/ITO antimony selenide solar cell, *Optik* 197 (2019) 16107.
- [22] R. Kumari, R. Kumar, V. Singh, SnTe as a BSF enhances the performance of Sb2Se3 based solar cell: a numerical approach, *Heliyon* 8 (2022) e12043.
- [23] A. Sunny, S.R. Al Ahmed, Numerical simulation and performance evaluation of highly efficient Sb2Se3 solar cell with tin sulfide as hole transport layer, *Phys. Status Solidi* 258 (2021) 2000630.
- [24] X. Wang, R. Tang, Y. Yin, H. Ju, C. Zhu, T. Chen, Interfacial engineering for high efficiency solution processed Sb2Se3 solar cells, *Sol. Energy Mater. Sol. Cells* 189 (2019). 5–10.
- [25] Mamta, Y. Singh, K.K. Maurya, V.N. Singh, n-Si/p-Sb2Se3 structure based simple solar cell device, *Mater. Today Sustain.* 18 (2022) 100148.
- [26] N. Torabi, E. Artigiani, A. Gasparotto, F. Piccinelli, M. Meneghini, G. Meneghesso, A. Romeo, Analysis of CdSe as an alternative buffer layer for Sb2Se3 solar cells, *Sol. Energy* 264 (2023) 111990.
- [27] Mamta, K.K. Maurya, V.N. Singh, Sb2Se3 versus Sb2S3 solar cell: a numerical simulation, *Sol. Energy* 228 (2021) 540–549.
- [28] K. Maurya Mamta, V. Singh, Influence of buffer layers on antimony selenide based solar cell, *Opt. Mater.* 126 (2022) 112240.
- [29] A.T. Ngoupo, S. Ouédraogo, F. Zougmoré, J.-M.B. Ndjaka, Numerical analysis of ultrathin Sb2Se3-based solar cells by SCAPS-1D numerical simulator device, *Chin. J. Phys.* 70 (2021) 1–13.
- [30] I. Gharibshahian, A.A. Orouji, S. Sharbatli, Effect of the junction barrier on current-voltage distortions in the Sb2Se3/Zn(O,S) solar cells, *Opt. Mater.* 116 (2021).
- [31] Mamta, K.K. Maurya, V.N. Singh, Enhancing the performance of an Sb2Se3-based solar cell by dual buffer layer, *Sustainability* 13 (2021).
- [32] I. Gharibshahian, A.A. Orouji, S. Sharbatli, Alternative buffer layers in Sb2Se3 thin-film solar cells to reduce open-circuit voltage offset, *Sol. Energy* 202 (2020) 294–303.
- [33] Z. Ali, K. Ali, B. Hussain, S. Maqsood, I. Iqbal, Towards the enhanced efficiency of ultrathin Sb2Se3 based solar cell with cubic silicon carbide (3C-SiC) buffer layer, *Opt. Mater.* 128 (2022) 112358.
- [34] G. Li, Z. Li, X. Liang, C. Guo, K. Shen, Y. Mai, Improvement in Sb2Se3 solar cell efficiency through band alignment engineering at the buffer/absorber interface, *ACS Appl. Mater. Interfaces* 11 (2019) 828–834.
- [35] A. Teyon Ngoupo, J.-M.B. Ndjaka, Performance enhancement of Sb2Se3-based solar cell with hybrid buffer layer and MoSe2 as a hole transport material using simulator device, *Discover Mechanical Eng.* 1 (.5) (2022).
- [36] H. Jalali, A.A. Orouji, I. Gharibshahian, Controlled conduction band offset in Sb2Se3 solar cell through introduction of (Zn,Sn)O buffer layer to improve photovoltaic performance: a simulation study, *Sol. Energy Mater. Sol. Cells* 260 (2023) 112492.
- [37] K.T. Arockiya-Dass, K. Sekar, L. Marasamy, Theoretical insights of degenerate ZrS2 as a new buffer for highly efficient emerging thin-film solar cells, *Energy Technol.* 11 (2023) 2300333.
- [38] B. Maharana, R. Jha, S. Chatterjee, Metal oxides as buffer layers for CZTS based solar cells: a numerical analysis by SCAPS-1D software, *Opt. Mater.* 131 (2022) 112734.
- [39] M. Moustafa, B. Mourched, S. Salem, S. Yasin, Performance enhancement of CZTS-based solar cells with tungsten disulfide as a new buffer layer, *Solid State Commun.* 359 (2023) 115007.
- [40] A. Basak, S. Padhy, U.P. Singh, Antimony chalcogenides based thin-film solar cell, in: *Recent Advances in Thin Film Photovoltaics*, Springer, 2022, pp. 151–178.
- [41] J. Dong, Y. Liu, Z. Wang, Y. Zhang, Boosting VOC of antimony chalcogenide solar cells: a review on interfaces and defects, *Nano Select* 2 (2021) 1818–1848.
- [42] A.A. Abdelaziz, M. Sahal, E. Oublal, N. Kumar, A. Benami, New Sb2Se3 based solar cell for achieving high efficiency-Theoretical modeling, *Opt. Quant. Electron.* 55 (2023) 514.
- [43] M.K.S. Bin Rafiq, N. Amin, H.F. Alharbi, M. Luqman, A. Ayob, Y.S. Alharthi, N. H. Alharthi, B. Bais, M. Akhtaruzzaman, WS2: a new window layer material for solar cell application, *Sci. Rep.* 10 (2020) 771.
- [44] R. Huang, M. Yu, Q. Yang, L. Zhang, Y. Wu, Q. Cheng, Numerical simulation for optimization of an ultra-thin n-type WS2/p-type c-Si heterojunction solar cells, *Comput. Mater. Sci.* 178 (2020).
- [45] S.R. Al Ahmed, M. Rahaman, A. Sunny, S. Rahman, M.S. Islam, T.A.E.-M. Taha, Z. Alrowaili, M.S. Mian, Enhancing the efficiency of Cu2Te thin-film solar cell with WS2 buffer layer: a simulation study, *Opt. Laser. Technol.* 159 (2023) 108942.
- [46] N. Rai, S. Rai, P.K. Singh, P. Lohia, D.K. Dwivedi, Analysis of various ETL materials for an efficient perovskite solar cell by numerical simulation, *J. Mater. Sci. Mater. Electron.* 31 (2020) 16269–16280.
- [47] P. Dubey, Sadanand, S. Rai, B.K. Pandey, D.K. Dwivedi, Simulation engineering of heterojunction colloidal quantum dot- solar cell using tungsten trioxide (WO3) as an electron transport layer, in: A. Dhawan, R.A. Mishra, K.V. Arya, C. R. Zamarréno (Eds.), *Advances in VLSI, Communication, and Signal Processing*, Springer Nature Singapore, Singapore, 2022, pp. 223–231.

- [48] J.C.Z. Medina, E.R. Andrés, C.M. Ruiz, E.C. Espinosa, L.T. Yarce, R. Galeazzi Isasmendi, R.R. Trujillo, G.G. Salgado, A.C. Solis, F.G.N. Caballero, Numerical simulation and performance optimization of a solar cell based on WO₃/CdTe heterostructure using NiO as HTL layer by SCAPS-1D, *Coatings* 13 (2023) 1436.
- [49] K. Sobayel, M. Akhtaruzzaman, K.S. Rahman, M.T. Ferdaous, Z.A. Al-Mutairi, H. F. Alharbi, N.H. Alharthi, M.R. Karim, S. Hasmady, N. Amin, A comprehensive defect study of tungsten disulfide (WS₂) as electron transport layer in perovskite solar cells by numerical simulation, *Results Phys.* 12 (2019) 1097–1103.
- [50] K. Sobayel, M. Shahinuzzaman, N. Amin, M.R. Karim, M.A. Dar, R. Gul, M. A. Alghoul, K. Sopian, A.K.M. Hasan, M. Akhtaruzzaman, Efficiency enhancement of CIGS solar cell by WS₂ as window layer through numerical modelling tool, *Sol. Energy* 207 (2020) 479–485.
- [51] L.R. Karna, R. Upadhyay, A. Ghosh, All-inorganic perovskite photovoltaics for power conversion efficiency of 31, *Sci. Rep.* 13 (2023) 15212.
- [52] M. Modak, S. Rane, S. Jagtap, WO₃: a review of synthesis techniques, nanocomposite materials and their morphological effects for gas sensing application, *Bull. Mater. Sci.* 46 (2023) 28.
- [53] X. He, Y. Iwamoto, T. Kaneko, T. Kato, Fabrication of near-invisible solar cell with monolayer WS₂, *Sci. Rep.* 12 (2022) 11315.
- [54] F.G. Aras, A. Yilmaz, H.G. Tasdelen, A. Ozden, F. Ay, N.K. Perkgoz, A. Yeltik, A review on recent advances of chemical vapor deposition technique for monolayer transition metal dichalcogenides (MX₂: Mo, W; S, Se, Te), *Mater. Sci. Semicond. Process.* 148 (2022) 106829.
- [55] J. Gutpa, H. Shaik, K.N. Kumar, S.A. Sattar, PVD techniques proffering avenues for fabrication of porous tungsten oxide (WO₃) thin films: a review, *Mater. Sci. Semicond. Process.* 143 (2022) 106534.
- [56] Y. Yao, D. Sang, L. Zou, Q. Wang, C. Liu, A review on the properties and applications of WO₃ Nanostructure-Based optical and electronic devices, *Nanomaterials* 11 (2021) 2136.
- [57] M. Burgelman, P. Nollet, S. Degrave, Modelling polycrystalline semiconductor solar cells, *Thin Solid Films* 361 (2000) 527–532.
- [58] M.A. Rahman, Numerical modeling of ultra-thin CuSbS₂ heterojunction solar cell with TiO₂ electron transport and CuAlO₂:Mg BSF layers, *Opt. Mater. Express* 12 (2022) 2954–2973.
- [59] F. Baig, Y.H. Khattak, A. Shuja, K. Riaz, B.M. Soucase, Performance investigation of Sb₂Se₃ based solar cell by device optimization, band offset engineering and Hole Transport Layer in SCAPS-1D, *Curr. Appl. Phys.* 20 (2020) 973–981.
- [60] E. Karimi, S.M.B. Ghorashi, The effect of SnO₂ and ZnO on the performance of perovskite solar cells, *J. Electron. Mater.* 49 (2019) 364–376.
- [61] M.K. Sobayel, M.S. Chowdhury, T. Hossain, H.I. Alkhannash, S. Islam, M. Shahiduzzaman, M. Akhtaruzzaman, K. Techato, M.J. Rashid, Efficiency enhancement of CIGS solar cell by cubic silicon carbide as prospective buffer layer, *Sol. Energy* 224 (2021) 271–278.
- [62] D.A. Fentahun, A. Tyagi, K.K. Kar, Numerically investigating the AZO/Cu₂O heterojunction solar cell using ZnO/CdS buffer layer, *Optik* 228 (2021).
- [63] F. Marangi, M. Lombardo, A. Villa, F. Scotognella, (INVITED) new strategies for solar cells beyond the visible spectral range, *Opt. Mater. X* 11 (2021) 100083.
- [64] C. Chen, X. Xie, M. Yang, H. Zhang, I. Seok, Z. Guo, Q. Jiang, G. Wangila, Q. Liu, Recent advances in solar energy full spectrum conversion and utilization, *ES Energy & Environ.* 11 (2021) 3–18.
- [65] B.K. Mondal, S.K. Mostaque, M.A. Rashid, A. Kuddus, H. Shirai, J. Hossain, Effect of CdS and In₃Se₄ BSF layers on the photovoltaic performance of PEDOT:PSS/n-Si solar cells: simulation based on experimental data, *Superlattice. Microst.* 152 (2021).
- [66] R. Kumari, Mamta, A.K. Chaudhary, V.N. Singh, Performance analysis of CdS-free, Sb₂Se₃/ZnSe p-n junction cells with various hole transport layers and contacts, *Adv. Theory and Simulations*, n/a (2023) 2300322.
- [67] T. Ablekim, E. Colegrave, W.K. Metzger, Interface engineering for 25% CdTe solar cells, *ACS Appl. Energy Mater.* 1 (2018) 5135–5139.
- [68] M.D. Haque, M.H. Ali, M.F. Rahman, A.Z.M.T. Islam, Numerical analysis for the efficiency enhancement of MoS₂ solar cell: a simulation approach by SCAPS-1D, *Opt. Mater.* 131 (2022) 112678.
- [69] A. Bag, R. Radhakrishnan, R. Nekovei, R. Jeyakumar, Effect of absorber layer, hole transport layer thicknesses, and its doping density on the performance of perovskite solar cells by device simulation, *Sol. Energy* 196 (2020) 177–182.
- [70] R. Malani, T. Pansuriya, V. Kheraj, A study on influence of potential defects and optimization of device structure for CuSbS₂ based thin film solar cell using SCAPS – 1D simulator, *Opt. Mater.* 133 (2022) 112910.
- [71] H. Kafashan, A. Bahrami, CIGS solar cells using ZrS₂ as buffer layer: numerical simulation, *Optik* (2023) 171594.
- [72] S.R.I. Biplob, M.H. Ali, M.M.A. Moon, M.F. Pervez, M.F. Rahman, J. Hossain, Performance enhancement of CIGS-based solar cells by incorporating an ultrathin BaSi₂ BSF layer, *J. Comput. Electron.* 19 (2019) 342–352.
- [73] M.M. Khutun, A. Sunny, S.R. Al Ahmed, Numerical investigation on performance improvement of WS₂ thin-film solar cell with copper iodide as hole transport layer, *Sol. Energy* 224 (2021) 956–965.
- [74] M.A. Hachimi, A. Tarbi, M. El Mrabet, H. Erguig, T. Chtouki, Performance and stability optimization of CsPbCl₃-yI (y = 0, 1, 2, and 3) lead-based perovskites solar cells using SCAPS-1D, *J. Phys. Chem. Solid.* 183 (2023) 111651.
- [75] I. Chabri, A. Oubelkacem, Y. Benhouria, A. Kaiba, I. Essaoudi, A. Ainane, Performance optimization of a CsGeI₃-based solar device by numerical simulation, *Mater. Sci. Eng., B* 297 (2023) 116757.
- [76] P. Würfel, U. Würfel, Physics of Solar Cells: from Basic Principles to Advanced Concepts, John Wiley & Sons, 2016.
- [77] A. Priya, S.N. Singh, Enhancement of efficiency and external quantum efficiency of CIGSSe solar cell by replacement and inserting buffer and Cu₂O ER-HTL layer, *Superlattice. Microst.* 152 (2021).
- [78] M.N. Sarder, M.A. Al Mamun, M.H. Ali, M.D. Haque, M.F. Rahman, A.Z.M. T. Islam, Numerical simulation of MoSe₂ based solar cell by SCAPS-1D, in: 2022 International Conference on Recent Progresses in Science, Engineering and Technology (ICRPSET), IEEE, 2022, pp. 1–5.
- [79] A. Gholami-Milani, S. Ahmadi-Kandjani, B. Olyaeefar, M.H. Kermani, Performance analyses of highly efficient inverted all-perovskite bilayer solar cell, *Sci. Rep.* 13 (2023) 8274.
- [80] S. Rahman, S.R.A. Ahmed, Photovoltaic performance enhancement in CdTe thin-film heterojunction solar cell with Sb₂S₃ as hole transport layer, *Sol. Energy* 230 (2021) .605–617.
- [81] T.M. Cheng, C.H. Cai, W.C. Huang, W.L. Xu, L.H. Tu, C.H. Lai, Efficiency enhancement of Cu_{(In,Ga)(S,Se)}₂ solar cells by indium-doped CdS buffer layers, *ACS Appl. Mater. Interfaces* 12 (2020) 18157–18164.
- [82] M.S. Rana, M.M. Islam, M. Julkarnain, Enhancement in efficiency of CZTS solar cell by using CZTSCs BSF layer, *Sol. Energy* 226 (2021) 272–287.
- [83] I. Gharibshahian, A.A. Orouji, S. Sharbatli, Efficient Sb₂(S,Se)3/Zn(O,S) solar cells with high open-circuit voltage by controlling sulfur content in the absorber-buffer layers, *Sol. Energy* 227 (2021) 606–615.
- [84] B. Marí Soucase, F. Baig, Y. Hameed Khattak, E. Vega, M. Mollar, Numerical analysis for efficiency limits of experimental perovskite solar cell, *Sol. Energy* 235 (2022) 200–208.
- [85] M.S. Islam, M.J. Rashid, M. Akhtaruzzaman, T. Suemasu, J. Kazmi, M.R. Karim, I. A. Alnaser, K. Sobayel, Exploration of Cd_{1-x}ZnxSe as a window layer for CIGS based solar cell with PEDOT: PSS as back surface field layer, *Mater. Res. Express* 10 (2023) 126405.
- [86] S. Tajima, H. Katagiri, K. Jimbo, N. Sugimoto, T. Fukano, Temperature dependence of Cu₂ZnSnS₄ photovoltaic cell properties, *APEX* 5 (2012) 82302.
- [87] S. Tajima, T. Itoh, H. Hazama, K. Ohishi, R. Asahi, Improvement of the open-circuit voltage of Cu₂ZnSnS₄ solar cells using a two-layer structure, *APEX* 8 (2015) 82302.
- [88] T. Minemoto, M. Murata, Theoretical analysis on effect of band offsets in perovskite solar cells, *Sol. Energy Mater. Sol. Cells* 133 (2015) 8–14.
- [89] M. Atowar Rahman, Performance analysis of WSe₂-based bifacial solar cells with different electron transport and hole transport materials by SCAPS-1D, *Heliyon* 8 (2022) e09800.
- [90] M. Deo, R.K. Chauhan, Tweaking the performance of thin film CIGS solar cell using InP as buffer layer, *Optik* 273 (2023) 170357.
- [91] S. Mushtaq, S. Tahir, A. Ashfaq, R.S. Bonilla, M. Haneef, R. Saeed, W. Ahmad, N. Amin, Performance optimization of lead-free MASnBr₃ based perovskite solar cells by SCAPS-1D device simulation, *Sol. Energy* 249 (2023) 401–413.
- [92] O. Savadogo, K.C. Mandal, Low cost Schottky barrier solar cells fabricated on CdSe and Sb₂S₃ films chemically deposited with silicotungstic acid, *J. Electrochem. Soc.* 141 (1994) 2871.
- [93] S.H. Cheragee, M.J. Alam, Device modelling and numerical analysis of high-efficiency double absorbers solar cells with diverse transport layer materials, *Results in Optics* 15 (2024) 100647.
- [94] S.R. Meher, L. Balakrishnan, Z.C. Alex, Analysis of Cu₂ZnSnS₄/CdS based photovoltaic cell: a numerical simulation approach, *Superlattice. Microst.* 100 (2016) .703–722.
- [95] Sadanand, P.K. Singh, S. Rai, P. Lohia, D.K. Dwivedi, Comparative study of the CZTS, CuSbS₂ and CuSbSe₂ solar photovoltaic cell with an earth-abundant non-toxic buffer layer, *Sol. Energy* 222 (2021) 175–185.
- [96] C. Tiwari, G.K. Gupta, V. Mishra, Computational analysis of lead free and highly efficient intrinsic Ch₃NH₃SnI₃ based solar cell with suitable transport layers, *Results in Optics* 13 (2023) 100517.
- [97] K. Yang, B. Li, G. Zeng, Sb₂Se₃ thin film solar cells prepared by pulsed laser deposition, *J. Alloys Compd.* 821 (2020) 153505.
- [98] I. Gharibshahian, A.A. Orouji, S. Sharbatli, Towards high efficiency Cd-Free Sb₂Se₃ solar cells by the band alignment optimization, *Sol. Energy Mater. Sol. Cells* 212 (2020) 110581.
- [99] X. Wen, Y. He, C. Chen, X. Liu, L. wang, B. Yang, M. Leng, H. Song, K. Zeng, D. Li, K. Li, L. Gao, J. Tang, Magnetron sputtered ZnO buffer layer for Sb₂Se₃ thin film solar cells, *Sol. Energy Mater. Sol. Cells* 172 (2017) 74–81.
- [100] Z. Li, X. Chen, H. Zhu, J. Chen, Y. Guo, C. Zhang, W. Zhang, X. Niu, Y. Mai, Sb₂Se₃ thin film solar cells in substrate configuration and the back contact selenization, *Sol. Energy Mater. Sol. Cells* 161 (2017) 190–196.